Evaluation of the quality of a UAV-based eddy covariance system for measurements of wind field and turbulent flux

Yibo Sun[1,2,3], Shaomin Liu[4], Xinwen Lin[5], Ziwei Xu[4], Bing Geng[6], Bo Liu[1,2,3], Shengnan Ji[1,2,3], Junping Jing[7], Zhiping Zhu[8,9], Bilige Sude[1,2,3], Zhanjun Quan[1,2,3]

[1]State Key Laboratory of Environmental Criteria and Risk Assessment, Chinese Research Academy of Environmental Sciences, Beijing 100012, China.
[2]Institute of Ecology, Chinese Research Academy of Environmental Sciences, Beijing 100012, China.
[3]State Environmental Protection Key Laboratory of Ecological Regional Processes and Functions Assessment, Beijing 100012, China.
[4]State Key Laboratory of Earth Surface Processes and Resource Ecology, Faculty of Geographical Science, Beijing Normal University, Beijing 100875, China.
[5]Collage of Geography and Environment Science, Zhejiang Normal University, Zhejiang 321004, China.
[6]Beijing Academy of Social Sciences, Beijing 100101, China.
[7]National Ocean Technology Center, Tianjin 300112, China.
[8]Kunming General Survey of Natural Resources Center, China Geological Survey, Kunming 650111, China.
[9]Technology Innovation Center for Natural Ecosystem Carbon Sink, Ministry of Natural Resources, Kunming 650100, China.

Correspondence to: Yibo Sun (sun.yibo@ craes.org.cn) and Shaoming Liu (smliu@bnu.edu.cn)

Abstract. Instrumentation packages of eddy covariance (EC) have been developed for a small unmanned aerial vehicle (UAV) to measure the turbulent fluxes of latent heat (LE), sensible heat (*H*), and CO_2 (*Fc*) in the atmospheric boundary layer. This study evaluates the measurement performance of this UAV-based EC system. First, the precision (1σ) of geo-referenced wind measurement was estimated at 0.07 m s^{-1}. Then, the effect of calibration parameter and aerodynamic characteristics of the UAV on the quality of the measured wind was examined by conducting a set of calibration flights. The results shown that the calibration improved the quality of measured wind field, and the influence of upwash and leverage effect can be ignored in the wind measurement. Third, for the measurement of turbulent fluxes, the measurement error caused by instrumental noise was estimated at 0.03 μmol m^{-2} s^{-1} for *Fc*, 0.02 W m^{-2} for *H*, and 0.08 W m^{-2} for LE. Fourth, data from the standard operational flights are used to assess the influence of resonance on the measurements and to test the sensitivity of the measurement under the variation (±30 %) of the calibration parameters around their optimum values. Results shown that the effect of resonance mainly affect the measurement of CO_2 (~5 %). The pitch offset angle (ε_θ) significantly affected the measurement of vertical wind (~30 %) and turbulent fluxes (~15 %). The heading offset angle (ε_ψ) mainly affected the measurement of horizontal wind (~15 %), and other calibration parameters had no significant effect on the measurements. The results lend confidence to use the UAV-based EC system, and suggest future directions for optimization and development of the next generation system.

1 Introduction

In environmental, hydrological and climate change sciences, the measurement of surface fluxes at the regional scale (level of several to tens of kilometers) has attracted great interest despite often being considered a gordian knot (Mayer et al., 2022; Chandra et al., 2022). Process-based or remote sensing (RS)-based models are often used to estimate land surface fluxes of matter and energy at continental to global scales with typical spatial resolution from 1-10 km (Hu and Jia, 2015; Mohan et al., 2020; Liu et al., 1999). However, observational data, especially at similar scales to models' estimates, is often lacking, which presents a significant challenge for the validation and evaluation of the surface flux products from these models' estimates (Li et al., 2018; Li et al., 2017). On the ground, in the past decades, extensive eddy-covariance (EC) flux sites with their composed networks and optical-microwave scintillometer (OMS) sites have been built to provide temporally continuous monitoring of surface flux at local (hundreds of meters around the measurement site of ground EC) and path (a distance of a few hundred meters to near 10 kilometers between transmitter and receiver terminal of OMS) scales (Yang et al., 2017; Liu et al., 2018; Zhang et al., 2021; Zheng et al., 2023). Generally speaking, flux from ground measurements need to be scaled up to kilometers-scale to provide comparable spatial surface "relative-truth" flux data for the process- or RS-based models at larger spatial scales (Liu et al., 2016). However, the spatial density of these flux measurements sites is still low compared to the heterogeneity of surface fluxes, which means that major scaling bias may exist in the upscaled flux data (Wang et al., 2016; Li et al., 2021). Therefore, regional-scaled flux measurement techniques need to be developed to complement the ground- and models-based approaches (Vellinga et al., 2010).

Aircraft-based EC flux measurement method, which has been developed for turbulence measurements for more than 40 years (Lenschow et al., 1980; Desjardins et al., 1982), is considered as the optimum method to measure turbulent flux at regional scale (several hundred square kilometers), thus bridging the scale gap between ground and model-derived methods (Gioli et al., 2004; Garman et al., 2006). To date, several types of aircrafts, including manned or unmanned fixed-wing aircrafts, delta-wing aircrafts, and helicopters, have been used for measurements of turbulent flux by equipping them with the EC sensors to measure three-dimensional (3D) wind, air temperature, and gas concentrations at a frequency of 50 Hz (Gioli et al., 2006; Metzger et al., 2012; Thomas et al., 2012; Bange and Roth, 1999). Among them, fixed-wing aircrafts and delta-wing aircrafts are better airborne platforms for EC measurements compared to helicopters due to their tightly coupled structure with the wind sensor and because their flow distortion around the fuselage can be more easily avoided or modeled (Prudden et al., 2018; Garman et al., 2008). A wide range of manned aircrafts has been developed to measure turbulent flux, including single-engine light aircrafts (e.g., Sky Arrow 650, Long-EC, WSMA) (Gioli et al., 2006; Crawford and Dobosy, 1992; Metzger et al., 2012), twin-engine aircrafts (e.g., Twin Otter, NASA CARAFE) (Desjardins et al., 2016; Wolfe et al., 2018) and larger quad-engine utility aircrafts (e.g., NOAA WP-3D) (Khelif et al., 1999). These airborne flux measurements, in combination with ground measurements, provide an excellent opportunity to produce regional-scaled, spatio-temporal continuous surface flux datasets that can improve our understanding of the processes of land-atmosphere interactions in regional and global change (Chen et al., 1999; Liu et al., 1999; Prueger et al., 2005). However, manned aircrafts are expensive to operate and maintain. Aviation safety and operational regulations require that manned aircrafts must fly above a minimum altitude (400 m above the highest elevation within 25 km on each side of the center line of the air route) and must avoid hazardous conditions such as icing or severe turbulence (Elston et al., 2015). The flow distortion induced by the aircraft itself (from the wings, fuselage, and the propellers) complicates the wind vector measurement from aircraft platform, which means that sophisticated correction procedures should be applied to compensate for the flow distortion effects (Elston et al., 2015; Williams and Marcotte, 2000; Drüe and Heinemann, 2013).

In recent years, interesting in unmanned aerial vehicle (UAV) platforms for atmospheric studies have been fast growing, especially because of their lower construction, operation, and maintenance costs compared with manned platforms. High-performance fixed-wing UAVs offer a high payload capacity (5-10 kg) and similar endurance (2-3 h) and operating altitude (up to 3500 m above the sea level) to manned aircrafts, but with much less turbulence disturbance due to their small fuselage size (Reineman et al., 2013). More importantly, the advancements in small, fast, and powerful sensors and microprocessors make it possible to use of UAVs for comprehensive atmospheric measurements (Sun et al., 2021a). Several types of UAVs with different turbulence measurement objectives have been developed and deployed, ranging from small payload capacity (e.g., 140 g SUMO) to medium (e.g., 1.5 kg M^2AV, 1.0 kg MASC) and large (e.g., 6.8 kg Manta, 5.6 kg ScanEagle) (Reuder et al., 2016; Båserud et al., 2016; Van Den Kroonenberg et al., 2012; Reineman et al., 2013). A comprehensive overview of the use of these UAVs for turbulence sampling can be found in Elston et al. (2015) and Sun et al. (2021a). For turbulence measurements, the UAVs were equipped with a commercial or custom multi-hole (5- or 9-hole) probe paired with an integrated navigation system (INS) to obtain the wind vector. Small and medium UAVs typically could only measure fast 3D wind vector and air temperature fluctuations for measurements of momentum and sensible heat flux, whereas, large UAVs were equipped with more types (e.g., radiation, optics, or gas concentration) and more accurate sensors for measurement of a larger range of meteorological properties including sensible and latent heat fluxes, CO_2 flux, radiation fluxes as well as surface properties (Reineman et al., 2013; Sun et al., 2021a). UAVs equipped with scientific instruments can be deployed in a variety of application environments and conditions. UAVs offer distinct advantages over manned aircraft in their ability to safely perform measurements and greatly reduce operational costs especially in low-altitude conditions (below 100 m above the ground level), which are optimal for measuring turbulent flux (Witte et al., 2017). Anderson and Gaston (2013) predict that UAVs will revolutionize the spatial data collection in ecology and meteorology.

EC method is a well-developed technology for directly measuring vertical turbulent flux (flux of sensible heat, latent heat and CO_2) within the atmospheric boundary layers (ABL) (Peltola et al., 2021). It requires accurate time (for ground tower) or spatial (for mobile platform) series of both the transported scalar quantity and the transporting turbulent wind. Each should be measured at sufficient frequency to resolve the flux contribution from small eddies (Vellinga et al., 2013). The measurement of the geo-referenced 3D wind vector, which is the prerequisite for EC measurements, is challenging for airborne platform. Airborne measurement of geo-referenced 3D wind is the vector sum between the aircraft velocity relative to the earth (inertial velocity) and the velocity relative to the air (relative wind vector, or true airspeed). Therefore, accurate measurements of the relative wind as well as the motion and attitude of the platform are essential to accurately measure the geo-referenced wind vector and turbulent flux (Metzger et al., 2011). Garman et al. (2006) estimated the measurement precision (1σ) of the vertical wind measurements of a commercial 9-hole turbulence probe (known as "Best Air Turbulence Probe", often abbreviated as the "BAT Probe") to be 0.03 m s^{-1} by combining the precision of the BAT Probe and the integrated navigation device. The BAT Probe is widely used on manned fixed-wing aircrafts, such as Sky Arrow 650 ERA (Environmental research aircraft), Beechcraft Duchess, and Diamond DA42, for turbulent flux measurement (Gioli et al., 2006; Garman et al., 2008; Sayres et al., 2017). A light delta-wing EC flux measurement aircraft developed by Metzger et al. (2011) reported a 1σ precision of wind measurement of 0.09 m s^{-1} for horizontal wind and 0.04 m s^{-1} for vertical wind using a specially customized five-hole probe (5HP). On this basis, in combination with a commercial infrared gas analyzer, the 1σ precision of flux measurement was 0.003 m s^{-1} for friction velocity, 0.9 W m^{-2} for sensible heat flux, and 0.5 W m^{-2} for latent heat flux (Metzger et al., 2012). The EC flux measurement from a UAV platform can now be achieved with a similar reliability to a manned platform. The Manta and ScanEagle UAV-based EC measurements developed by Reineman et al. (2013) achieved precise wind measurements (0.05 m s^{-1} for horizontal and 0.02 m s^{-1} for vertical wind) using a custom nine-hole probe and a commercial high precision integrated navigation system (INS), at a lower price and lighter weight than the commercial BAT probe. However, the onboard instrument packages for Manta and ScanEagle UAV are independent of each other in their measurements of turbulent and radiation flux, and the CO_2 flux measurement is lacking.

Inspired by these studies, Sun et al. (2021a) used a high-performance fuel-powered vertical take-off and landing (VTOL), fixed-wing platform to integrate the scientific payloads for EC and radiation measurements to obtain a comprehensive measurement of turbulent and radiation flux using an UAV. This UAV-based EC system measured turbulent fluxes of sensible heat, latent heat, and CO_2, as well as radiation including net radiation and upward- and downward-looking photosynthetically active radiation (PAR). This system was successfully tested in the Inner Mongolia of China and applied to measure the regional sensible and latent heat fluxes in the Yancheng coastal wetland in Jiangsu, China (Sun et al., 2021a; 2021b). During these field studies, the UAV-based EC measurements achieved a near consistent observational result compared with ground EC measurements (Sun et al., 2021b). However, some shortcomings in the developed UAV-based EC system were also identified. In particular, the noise effects from the engine and propeller were not fully isolated, resulting in high frequency noise in the measured scalars (air temperature, H_2O, and CO_2 concentration). This UAV-based EC system is being continuously improved (in Section 2.1) based on field measurements. However, there is no quantitative evaluation of the measurement precision of the wind field and turbulent flux as well as of the influence of the resonance noise from the UAV operation yet. Previous work using ground EC as a benchmark to assess the measurement performance of the UAV-based EC system has been disputed, due to difference in EC sensors, platforms, measurement height, and source areas (i.e., footprint), as well as the influence of surface heterogeneity, flux divergence, inversion layer and the stochastic nature of turbulence (Sun et al., 2021b; Wolfe et al., 2018; Hannun et al., 2020).

This study attempts to evaluate the performance of the UAV-based EC system developed by Sun et al. (2021a) in the measurement of wind field and turbulent flux. For these purposes, data from two field measurement campaigns, including a set of calibration flights and some standard operation flights, were used in this study. First, the current study investigated the quality of the measurement of geo-referenced wind vector including measurement error (1σ) and the improvements for wind measurement after system calibration. Second, using the measured data from standard operation flights, flux measurement error related to instrumental noise was estimated with a method proposed by Billesbach (2011). Errors propagated through the correction terms [i.e., Webb-Pearman-Leuning (WPL) correction for latent heat and CO_2 flux] were also included in our analysis (Webb et al., 1980; Kowalski et al., 2021). Then, the impacts of resonance noise on the measured scalar variance and the flux covariance were also estimated by comparing the real (co)spectra curve with the theoretical reference curve from Massman and Clement (2005). Lastly, the sensitivity of the measured geo-referenced wind vector and turbulent flux to the errors in the calibration parameters (determined by the calibration flight) were assessed by adding an error of ±30 % to their optimum calibration value.

2 Materials and Methods

2.1 The UAV-based EC system

The UAV platform used for EC measurement is a high-performance, fuel-powered VTOL, fixed-wing UAV, which has minimal requirements for the takeoff location and offers a high payload capacity of up to 10 kg. The UAV has a wing-span of 3.7 m, a fuselage length of 2.85 m, and a maximum take-off weight of 60 kg. The UAV engine is mounted in a pusher configuration, allowing for the turbulence probe to be installed directly on the nose of the UAV, minimizing or eliminating airflow contamination due to upwash and sidewash generated by the wings (Crawford et al., 1996). Control of the UAV is totally autonomous, and the pilots have the option to enable manual and semi-manual control in emergency conditions. The UAV has a cruise flight speed of 28 to 31 m s^{-1} with an endurance of almost 3 h, and it has a flight ceiling of up to 3800 m above the sea level. Detailed information on this UAV could be found in Sun et al. (2021a).

The flux payloads of the UAV-based EC system include a precision-engineered 5-hole pressure probe (5HP) for measurement of the true airspeed and the attack (α) and sideslip (β) angles of incoming flow relative to the UAV, a dual-antenna integrated navigation system (INS) for high accuracy measurement of UAV ground speed and attitude, an open path infrared gas analyzer (IRGA) for recording the atmospheric densities of CO_2 and water vapor, a fast temperature sensor for measurement of the fast temperature fluctuations, and a slow-response temperature probe for providing a mean air temperature reference. The sample rate is 50 Hz except for the slow-response temperature probe (1 Hz), yielding a turbulence horizontal resolution of approximately 1.2 m at a cruising speed of 30 m s^{-1}. The system was improved according to deficiencies identified after several field measurements with the following adjustments: 1) a laser distance measurement unit was mounted for measuring the distance between the UAV and the ground level, 2) the platinum resistance thermometer was replaced by a thermocouple (Omega T-type COCO-003; $\varnothing 0.075\ \mathrm{mm}$) for improving the resistance of the high-frequency temperature measurements to vibration noise from the engine, 3) the vibration isolator structure of the IRGA was improved, and 4) the original datalogger (CR1000X, Campbell, USA) was replaced with a lighter one (CR6, Campbell, USA). All the digital and analog signals from the sensor modules are stored and synchronized by the on-board datalogger, and the on-board scientific payloads are designed to be isolated from the electronic components of the UAV to ensure that any problems occurring would not jeopardize the safety of the UAV (Sun et al., 2021a).

In the present study, to estimate the measurement precision of the geo-referenced wind and turbulent flux, the sensor modules and their 1σ precision of the measured variables related to EC measurement were used, as presented in Table 1. For the 5HP, the 1σ measurement precision was acquired from the wind tunnel test after wind tunnel calibration (Sun et al., 2021a).

Table 1: Summary of the sensor modules, measured variables, and their measurement precision used to determine the geo-referenced wind velocity and turbulent flux.

Sensor (Module, company, country)	Variables	Precision ($\mathbf{1\sigma}$)
GNSS/INS (BD992-INS, Trimble, USA)	Roll, Pitch, Heading	0.1°
	Horizontal velocity	0.007 m s^{-1}
	Vertical velocity	0.02 m s^{-1}
5HP (ADP-55, Simtec AG, Switzerland)	Attack angle	0.02°#
	Sideslip angle	0.04°#
	True airspeed	0.05 m s^{-1}#
	Static pressure	1.1 hPa
	Dynamic pressure	0.003 hPa
IRGA (EC150, Campbell, USA)	CO_2 density	0.2 mg m^{-3}
	H_2O density	0.004 g m^{-3}
Thermistor (100K6A1IA, Campbell, USA)	Temperature (slow)	0.2 ℃
Thermocouple (T-type COCO-003, Omega, USA)	Temperature (fast)	0.5 ℃

Results from the wind tunnel test.

2.2 Field campaign

2.2.1 In-flight calibration campaign

In order to calibrate the wind measurement component of the UAV-based EC system, an in-flight calibration campaign was carried out on 4 September 2022 at the Caofeidian Shoal Harbor in the Bohai Sea of northern China. The average water depth of this area is approximately 0-5 m, with a maximum water depth of 22 m. At low tide, a large area of the tidal flat is exposed; while at high tide, only the barrier islands are visible (Xu et al., 2021). The assumptions for calibration flight include 1) low turbulent transport condition (i.e., no disturbance), 2) a constant mean horizontal wind, and 3) mean vertical wind near zero (Drüe and Heinemann, 2013; Vellinga et al., 2013; Van Den Kroonenberg et al., 2008). This allows identical wind components for several consecutive straights in opposite or vertical flight directions. These assumptions are usually well satisfied above the ABL or under stable atmospheric conditions (Drüe and Heinemann, 2013). Over the sea surface, due to its uniform and cool surface property, the turbulence fluctuations are weaker than that over the land surface (Mathez and Smerdon, 2018), making where a more ideal environment to conduct calibration flight.

The in-flight calibration campaign included three flight maneuvers, including a 'box' maneuver, 'racetrack' maneuver, and 'acceleration-deceleration' maneuver. The trajectory of the calibration flight is shown in Figure 1, with different color corresponding to different flight maneuver. The calibration flight was executed between 7:28-7:48 a.m. (China Standard Time, CST) to coincide with the ebb tide stage. During this time, the average water depth was approximately 1.1 m, and the average flight altitude was 400 m ($\sigma = \pm 0.78$ m) above the sea level. Considering the uniform and cool underlying surface and the stable atmospheric conditions in the early morning, we assume no disturbance from underlying surface was present during the calibration flight.

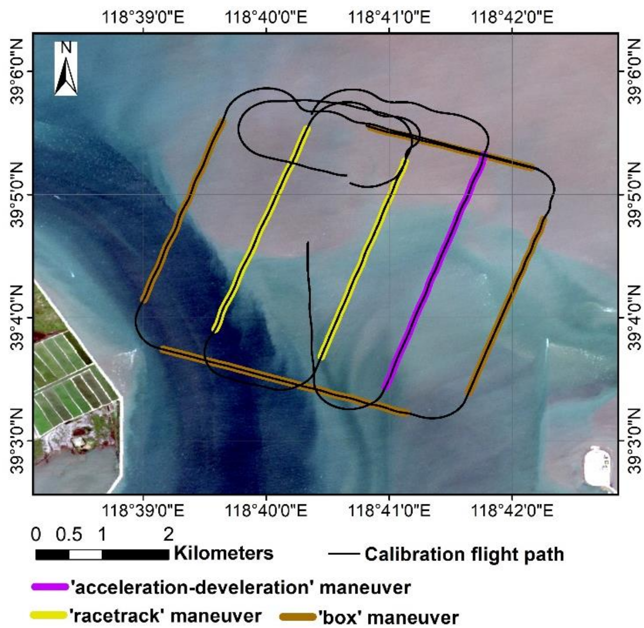

Figure 1. Flight trajectory of the calibration campaign on 4 September 2022 at the Caofeidian Shoal Harbor in the Bohai Sea of northern China. The land surface image is from Sentinel-2A satellite image with true color combination acquired on 1 September 2022.

In this study, the 'box' maneuver is used to determine the mounting misalignment angle in the heading (ϵ_{ψ}) and pitch (ϵ_{θ}) between the 5HP and the center of gravity (CG) of the UAV. The flight path is a box in which the four straight legs are flown at constant cruising speed, flight altitude, and heading for 2 minutes. The 'racetrack' maneuver is used to evaluate the quality of the calibration parameters acquired from the previous 'box' maneuver. The flight path consists of two parallel straight flight tracks connected by two 180^{o} turns. Each straight flight section lasts 2 minutes at constant speed and flight altitude. Lastly, the 'acceleration-deceleration' maneuver is used to check the influence of lift-induced upwash from the wing to the measured attack angle by the 5HP. During this maneuver, the aircraft is kept straight and level at constant pressure altitude. When beginning this maneuver, the aircraft accelerates to its maximum airspeed (35 m s^{-1}). Then, the airspeed reduces gradually to near its minimum airspeed (25 m s^{-1}) and back up to its maximum airspeed. The pressure-altitude of the aircraft is maintained throughout this maneuver, and the entire maneuver lasts one minute. This maneuver creates a series continuous changed pitch

(θ) and attack (α) angle. A relationship between the measured incident flow attack angles (α) by the 5HP and the measured pitch angle by the INS of close to 1:1, indicates that the effect from the fuselage-induced flow distortion on the wind measurements is negligible (Garman et al., 2006).

2.2.2 Standard operation flight campaign

The reliability of the EC measurement from UAV is susceptible to several factors, mainly including instrumental noise, resonance noise, and the quality of the calibration parameter. In order to evaluate the flux measurement error related to instrumental noise, the effects of resonance on the measured scalar and to investigate the sensitivity of the measured geo-referenced wind and turbulent flux to uncertainty in the calibration parameter, we used data from 7 flights in the Dagang district in Tianjin, China between 8 and 16 August 2022. This area is located on the west coast of the Bohai Sea and is a coastal alluvial plain with altitudes between 1-3 m (Chen et al., 2017). The flight path, shown in Figure 2, includes three parallel transect lines of approximately 4 km in length each and at 1-2 km intervals. All flights occurred during the daytime, and were performed in the same trajectory at low altitude about 90 m above sea level. The flight area covered three different underlying surfaces: land, coastal zone, and water surfaces, that can represent typical flux intensity characteristics for different surface conditions.

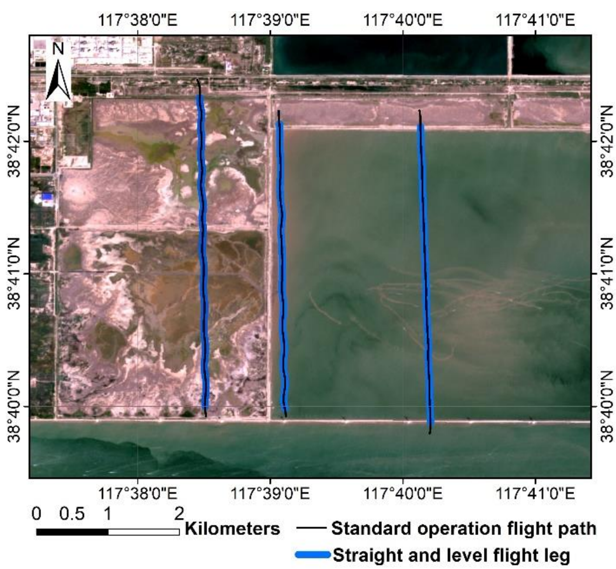

Figure 2. Flight trajectory of the standard operation flight campaign, 8-16 August 2022, at Dagang district, Tianjin, China. The land surface image is from Sentinel-2A satellite image with true color combination acquired on 27 August 2022.

During the operation flight campaign, the atmospheric stability conditions changed from stable (Monin-Obukhov stability parameter, $z/L = 1.93$) to very unstable ($z/L = -10.28$) as measured by the UAV, where z is the flight height above the ground level, L is the Obukhov length. The stable condition mostly occurred on flight path located over the sea surface, while the unstable condition mostly occurred on flight path located over the land surface. These flight data provide various measurement conditions for us to evaluate the performance of the UAV-based EC system.

2.3 Data processing

The raw data collected with the on-board datalogger (CR6, Campbell, USA) is subsequently saved in Network Common Data Form (netCDF) format. It includes dynamic and static pressure, attack, and sideslip angle of incoming flow; slow (1 Hz) and fast (50 Hz) air temperature; mass concentration of H_2O and CO_2; as well as the full navigation data (including 3D location, ground speed, angular velocity, and attitude, etc.) of the UAV. The subsequent data processing includes three basic processing stages in order to calculate flux data from raw measured data.

In the first stage, a moving average filter was used to detect outliers in each variable. Detected outliers were removed and replaced by values obtained by linear interpolation. Outliers tend to be rare. However, if outliers constitute more than 20 % of the data points, the corresponding flight data should be discarded. The cleaned raw data was then used to calculate the geo-referenced wind vector, (co)spectra, and turbulent fluxes.

In the second stage, geo-referenced 3D wind vector is calculated. The full form of the equations of motion for calculating the geo-referenced wind vector by the UAV-based EC system is described in detailed in Supplement Part A. From the aircraft platform, geo-referenced wind vector is measured in two independent reference coordinate systems: the relative true airspeed ($\widehat{U}_a$) measurement in the aircraft coordinate system and the ground speed of the aircraft (U_p) in the geo-referenced coordinate system. The geo-referenced wind (U) is the vector sum of the relative true airspeed ($\widehat{U}_a$), the UAV's motion (U_p) and the tangential velocity due to the rotational motion of the aircraft ("lever arm" effect), which is described in Eq. (S2). In this stage, the acquired calibration parameters (ϵ_ψ and ϵ_θ) from the calibration flight are substituted into the Eq. (S8) to correct the mounting angle offset errors between the 5HP and the CG of the UAV. The final equations for geo-referenced wind vector calculation (Eqs. S15 to S17) revealed that the lever arm effects due to the spatial separation between the tip of the wind probe and the CG of UAV can influence the wind measurements. Typically, the separation distance (L) is small, and the influence of the lever arm effects can be ignored when the L is less than about 10 m (Lenschow, 1986). In the current UAV-based EC system, the displacements of the 5HP tip with respect to the CG of the UAV along the three axes of UAB body coordinate are: $x^b = 1.459$ m, $y^b = 0$ m, and $x^b = 0.173$ m (in Supplement Part A). Therefore, in practice, the influence of leverage effects in geo-referenced wind calculation was also ignored in this study. This was confirmed by assessing the difference in the geo-referenced wind vector with and without the leverage effect correction term (in Section 3.1).

In the final stage, based on the EC technology and spatial averaging, the turbulent flux is calculated using the covariances of vertical wind (w) with air temperature (T_a) for sensible heat flux (H), with water vapor density (q) for latent heat flux (LE), and with CO_2 density (c) for CO_2 flux (F_c), and with the necessary correction (Webb et al., 1980). The time lag due to the separation between the 5HP tip, the adjacent temperature probe, and the open-path gas analysis did not need to be corrected because the time delay was less than 1 second at the cruise airspeed of 30 m s^{-1} and sensor separation less than 20 cm. Only the measurement data from the straight-line portion of the flight path can be used in flux calculation. Detailed calculation procedure and formulas of H, LE, and F_c used by the present UAV-based EC system are provided in Supplement Part B, including spatially averaging, coordinate rotation, and necessary correction (i.e., WPL correction for LE and F_c).

One important aspect for airborne EC measurement is the definition of a proper spatial averaging length to calculate turbulent flux (Sun et al., 2018). Such spatial averaging length depends on the flying altitude, surface characteristics, and atmospheric stability, and could be determined using Ogive analysis (Gioli et al., 2004; Kirby et al., 2008). In this study, the entire measured data of each straight and level flight leg (each with length about 4 km) from the standard operational flight campaign was used to calculate turbulent flux, regardless of the uncertainty in fluxes associated with spatial averaging.

2.4 Evaluation scheme

2.4.1 Wind measurement evaluation

The key to successful aircraft EC measurements lies in the translation of accurately measured, aircraft-orientated, wind vector to geo-referenced orthogonal wind vector (Thomas et al., 2012). Determining the geo-referenced wind vector requires a sequence of thermodynamic and trigonometric equations (Metzger et al., 2012), these equations propagate various sources of error to the measured geo-referenced wind vector. To estimate the measurement errors in the geo-referenced wind vector, we used the linearized Taylor series expansions of Eqs. (S15) to (S17) derived by Enriquez and Friehe (1995) (in Supplement Part A) to determine the sensitivities of each of the geo-referenced wind vector components with respect to the relevant variables. Then, these sensitivity terms can be combined to compute the overall measurement error (1σ) in the geo-referenced 3D wind vector (Eqs. S21 to S23 in Supplement Part A).

The above wind measurement error analysis gives the nominal measurement precision of the geo-referenced wind, but does not consider the influence of environmental changes. Following the methods of Lenschow and Sun (2007), we assess whether the accuracy of wind measurements from the UAV in satisfying the minimum signal level needed for resolving the mesoscale variations of the three wind components in the encountered atmospheric conditions. Firstly, the minimum required signal level for measurement of vertical air speed (ω) under the encountered atmospheric conditions could be estimated as (Lenschow and Sun, 2007):

$$\frac{\partial w}{\partial t} < 0.2\sqrt{2}\sigma_w 2\pi k U_a \qquad (1)$$

with the true airspeed (U_a) set to mean cruise speed 30 m s^{-1}, the peak signal magnitude (σ_w) of the power spectra, and the corresponding wavenumber (k) (Thomas et al., 2012). The measurement error of the system in the vertical wind component can be calculated as (Lenschow and Sun, 2007):

$$\frac{\partial w}{\partial t} \cong \Theta \frac{\partial U_a}{\partial t} + U_a \frac{\partial \Theta}{\partial t} + \frac{\partial w_{UAV}}{\partial t} \qquad (2)$$

with $\Theta = \alpha - \theta$, where α is the attack angle, θ is the pitch angle, w_{UAV} is the UAV's vertical velocity. According to Lenschow and Sun (2007), the signal level and mesoscale fluctuation of horizontal wind components (u and v) are considerably larger than that of vertical wind, so the accuracy criteria are not nearly as stringent. The measurement error of the horizontal wind component could be calculated as (Lenschow and Sun, 2007):

$$\frac{\partial u}{\partial t} \cong -\frac{\partial U_a}{\partial t} + \frac{\partial u_{UAV}}{\partial t} \tag{3}$$

$$\frac{\partial v}{\partial t} \cong \Psi \frac{\partial U_a}{\partial t} + v_{tas} \frac{\partial \Psi}{\partial t} + \frac{\partial v_{UAV}}{\partial t} \tag{4}$$

and,

$$\Psi \equiv \psi' + \beta \tag{5}$$

where u_{UAV}, v_{UAV} are the UAV's horizontal velocity measured from INS, ψ' is the departure of the measured true heading from the average true heading, and β is the sideslip angle of airflow. If the measurement error of the 3D wind vector from Eqs. (2) to (4) is smaller than the required minimum signal level of the vertical and horizontal wind components, it can be confirmed that the measurement accuracy of the geo-referenced 3D wind vector from UAV is sufficient to resolve the mesoscale variations of the three wind components in the encountered atmospheric conditions.

In addition, accurate measurements of geo-referenced wind vector typically not only depend on the measurement precision of the sensors (i.e., 5HP and INS), but also related to the quality of the calibration parameters and the geometry structure of the UAV EC system (i.e., flow distortion and leverage effect). For evaluation of the effect of the latter two aspects, a calibration flight campaign (Section 2.2.1) was performed to determine the calibration parameter ($\epsilon_{\psi}, \epsilon_{\theta}$), check its quality, as well as to ascertain the effects of the lever arm and up-wash by the wings. The methods for acquiring the calibration parameter were given by Vellinga et al. (2013) and Sun et al. (2021a), and the results are reported in Supplement Part C (Figs. S2 and S3). During the in-flight calibration campaign, a 'racetrack' maneuver was performed to check the quality of the calibration parameters determined from the 'box' flight maneuver. The initial ($\epsilon_{\psi} = 0°, \epsilon_{\theta} = 0°$) and calibrated ($\epsilon_{\theta} = -0.183°, \epsilon_{\psi} = 2°$, in Supplement Part C) set of parameters were used to calculate the geo-referenced wind vector. By comparing the mean and standard deviation of the horizontal and vertical wind vector between the initial and calibrated set, the quality of the geo-referenced wind vector measurement in real environment conditions can be verified.

The relative wind vector ($\widehat{U}_a$) measured by the aircraft is susceptible to flow distortion because the airplane must distort the flow to generate lift and thrust, and the aircraft's propellers, fuselage, and wings are the main sources of flow distortion as flow barriers (Metzger et al., 2011). For fixed-wing aircrafts, the wind probe mounted on the nose of the UAV and extended as far forward of the fuselage as possible could avoid significant influence from flow distortion from the fuselage and propellers. Nevertheless, effects from the induced upwash by the wings can also significantly influence the correspondence between measured and free-stream flow variables (Garman et al., 2008). The induced upwash by the wings modifies the local angle of attack, causing the measured attack angle (α) to be larger than the free-stream attack angle (α_{∞}). The magnitude of upwash influence generally increases with airplane size and airspeed, typically ranging from 0.5 to 2.5 m s^{-1} as reported by the manned fixed-wing aircraft (Garman et al., 2008). Therefore, for wind measurements by manned fixed-wing aircrafts, the upwash effects must be corrected (Garman et al., 2008; Kalogiros and Wang, 2002). However, wind measurements using a multi-hole probe on the UAV seldom need this correction due to the fuselage size and because the airspeed is very low compared to a manned aircraft.

In order to access whether the lift-induced upwash could be safety ignored by the current UAV-based EC system, the 'acceleration-deceleration' flight maneuver was performed. According to Crawford et al. (1996), the pitch angle (θ) by the INS instrument can be utilized as an estimate of the free-stream attack angle (α_∞) if the aircraft's vertical velocity is zero, since it is unaffected by lift-induced upwash and varies directly with α_∞ when the ambient vertical wind is zero. Under ideal conditions (zero aircraft vertical velocity and zero ambient vertical wind), the approximation relationship of $\theta \cong \alpha_\infty$ is valid when $\theta < 6°$ (Crawford et al., 1996; Vellinga et al., 2013). Departures from the 1:1 relationship can be caused by airflow distortion around the airplane behind the 5HP. The 'acceleration-deceleration' maneuver produced various pitch and attack angles measured under various airspeeds, which allowed a direct comparison between the pitch angle (θ) and the attack angle (α). If the slope between α and θ is close to unity, it indicates that the influence of lift-induced upwash can be ignored; otherwise, its influence should be corrected using upwash models (Garman et al., 2006). Meanwhile, the influence of leverage effects was also evaluated based on the measurement data from the 'acceleration-deceleration' maneuver by considering or ignoring the leverage effect correction term in Eqs. (S15) to (S17).

2.4.2 Flux measurement error caused by instrumental noise

Errors or uncertainties in EC measurements can be systematic or random. Measurement from UAV, they can be attributed to several sources, mainly including instrumental noise, data handing, atmospheric conditions, insufficient flux calculation length, and bumpy flight environment (Mahrt, 1998; Finkelstein and Sims, 2001; Mauder et al., 2013). Knowledge of the measurement precision is of great importance for interpretation of EC measurements especially when detecting small fluxes in terms of turbulent exchange or signal-to-noise (SNR) of the instrumentation. Determination of the flux measurement error from instrument noise is very useful, as it is related not only to the system performance, but also to the minimum resolvable capability for the flux to be measured. In the current study, uncertainty related to instrumental noise (listed in Table 1) was estimated with a directly method proposed by Billesbach (2011). This method can be called as "random shuffle" (denoted as the RS) method and was "designed to only be sensitive to random instrument noise". According to Billesbach (2011), the uncertainty of the flux covariance can be expressed as:

$$\sigma_{\overline{w'x'}} = \frac{1}{N}\sum_{i,j=1}^{N} w'(t_i)x'(t_j) \tag{6}$$

where x is the target entity of the covariance, N is the number of measurements contained in the block averaging period, $j \in [1 \ldots N]$ but the values are in the random order. The idea behind the RS method was that the randomly shuffled will remove the covariance between biophysical (source/sink) and transport mechanisms, leaving only the random "accidental" correlations attributed mostly to instrument noise (Billesbach, 2011). It means that the shuffled component x makes it uncorrelated in time/space and decorrelates x from w, resulting in two independent variables (i.e., $\overline{w'x'}\sim 0$), and any residual value of the covariance is attributed to random instrument noise. In addition to the basic assumptions made in EC flux calculation, one additional assumption in RS method is that the block averaging period should be sufficiently long to accurately represent the lowest significant frequencies contributing to the covariance which could be verified by forming Ogive plots of the covariance (Billesbach, 2011).

In this study, in order to obtain robust estimates of the instrumental noise, $\sigma_{\overline{w'x'}}$ was repeatedly calculated 20 times for every straight and level flight leg in operation flight (Fig. 2), and the mean of the absolute values of these 20 replicated estimates for $\sigma_{\overline{w'x'}}$ were used to estimate the random uncertainty related to instrumental noise. According to Rannik et al. (2016), RS method tends to overestimate the covariance uncertainty due to instrumental noise only. Then, the uncertainty in the flux covariance of sensible heat ($\sigma_{\overline{w'T'}}$), latent heat ($\sigma_{\overline{w'\rho'_v}}$), and CO_2 ($\sigma_{\overline{w'\rho'_c}}$) were estimated using RS method, respectively.

It should be noted that the measurement error of EC flux measurement is influenced not only by the uncertainty in the raw covariance but also by the propagated errors form correction terms (i.e., WPL correction) or any lens contamination (Serrano-Ortiz et al., 2008). For EC measurement from our UAV, the signal quality of the IRGA is checked before each flight measurement to ensure that the measurement of gas concentration is not affected by lens contamination. The final uncertainty of flux measurement was evaluated using the partial derivatives of the full flux calculation equation with respect to their flux value derived by Liu et al. (2006) (Eqs. S29 to S31 in Supplement Part B). These equations (Eqs. S29 to S31) ignored the perturbations terms from the errors in the individual scalar (i.e., ρ_v, ρ_c, T) which were proved negligible small (Serrano-Ortiz et al., 2008). At last, after several repetitive calculation of the Eq. (6), their averaged value then be combined to Eqs. (S29) to (S31) for estimating the final flux measurement error due to instrumental noise.

2.4.3 Resonance effects

Previous work found that the measurement of the atmospheric scalars (e.g., air temperature, H_2O, and CO_2 concentration) is susceptible to resonance effects caused by the operation of the engine and propeller (Sun et al., 2021b). In order to further reduce the resonance effects, the vibration damping structure of the developed UAV-based EC system was further optimized. The reference (co)spectra curve of Massman and Clement (2005) was used to quantify the influence of the resonance effects remaining after vibration isolation optimization. Massman and Clement (2005) gave the generalization mathematical expression of the models of spectra and co-spectra:

$$Co(f) = A_0 \frac{1/f_x}{[1+m(f/f_x)^{2\mu}]^{\frac{1}{2\mu}\left(\frac{m+1}{m}\right)}} \tag{6}$$

where f is frequency (Hz), f_x is the frequency at which $fCo(f)$ reaches its maximum value, A_0 is a normalization parameter, m is the (inertial subrange) slope parameter, and μ is the broadness parameter. To describe co-spectra, m should be 3/4; to describe spectra, m should be 3/2. According to Massman and Clement (2005), $\mu = 7/6$ under stable atmospheric condition and $\mu = 1/2$ under unstable atmospheric condition. Fast Fourier transform (FFT) method was used to calculate the spectra and co-spectra of the measured turbulent variables. Before calculating the turbulence (co)spectra, condition of the raw turbulence data was performed, including a linear detrend and tapering using the Hamming window to reduce the spectral leakage (sharp edge) according to Kaimal et al. (1989).

According to Sun et al. (2021b), the noise influence from resonance mainly appears in the high frequency domain. According to the feature of spectral curve, the frequency range of the noise region was artificially designated to $f > 8$ Hz for air temperature, $f = 1 \sim 5$ Hz for water vapor, and $f = 1 \sim 8$ Hz for CO_2. The normalized spectra and co-spectra curve were adopted and the area difference of the designated frequency range beneath the (co)spectra curve between the measured and reference (co)spectra curve was calculated to quantify the influence of resonance noise in the variance and flux covariance of the measurement atmosphere scalars. An example is shown in Figure 3, and also shown is the reference (co)spectra curve of Massman and Clement (2005), with the (co)spectral maximum at $f_x = 0.1$. The red region in Fig. 3 represents the impact extent of the resonance noise in the variance (Figs. 3a to 3c) and flux covariance (Figs. 3d to 3f) of the measured scalars. The systematic noise deviation in the fluxes of sensible, latent heat and CO_2 could be derived relative to the entire frequency range.

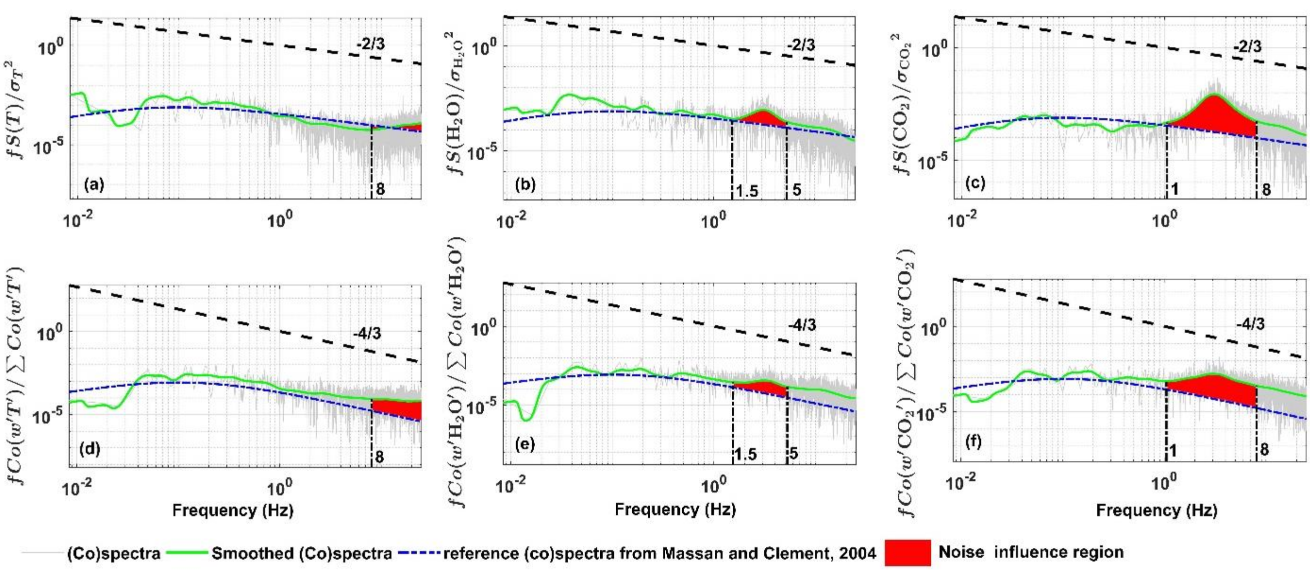

Figure 3. The influence of resonance noise on the spectra (top row) and co-spectra (bottom row) curve of the measured scalars based on the measurement from the standard operation flight campaign on 8 August 2022 at Dagang district, Tianjin, China. The red region is the area difference of the designated frequency range (vertical black dashed-dotted line) beneath the (co)spectral curve between the measured and reference (co)spectral curve.

2.4.4 Sensitivity analysis

To understand the relevance of the calibration parameters for the measurement of geo-referenced wind vector and turbulent flux, two sensitivity tests were conducted. The magnitude of the perturbation in the wind vector and turbulent flux was investigated as a function of the uncertainties in the four calibration parameters, including three mounting misalignment angles

($\epsilon_\psi, \epsilon_\theta, \epsilon_\phi$) between the 5HP and the CG of the UAV and one temperature recover factor ($\epsilon_r = 0.82$) used to calculate the ambient temperature (Eq. 3 in Sun et al. 2021a).

First, the sensitivity of the geo-referenced 3D wind vector and turbulent flux to the uncertainties of the individual parameter was investigated. The geo-referenced 3D wind vector and turbulent flux was calculated based on the straight leg (about 4 km) of the standard operational flight by adding an error of ± 30 % to the optimum value of each calibration parameter alternately; except for ϵ_ϕ, for which the typical range of $\pm 0.9°$ was taken for sensitivity analysis (Vellinga et al., 2013).

Then, in order to test the overall interaction between the parameters, a second sensitivity test was performed to calculate the geo-referenced 3D wind vector and turbulent fluxes by adding ± 30 % error to all calibration parameters simultaneously. Lastly, their relative errors (*RE*) with respect to the original value were calculated to evaluate the perturbation of the wind vector and turbulent flux under the variation of each calibration parameter as well as under simultaneous variation of all calibration parameters. During the sensitivity analysis, the calculated geo-referenced wind and turbulent flux results whose absolute value was less than their least resolvable magnitude were filtered out to avoid the influence of the errors contained in the measurements themselves on the results.

2.4.5 Relative error

In this study, relative error (*RE*) was used to evaluate the influence of different factors on the measurements of geo-referenced wind vector and turbulent flux by the UAV-based EC system. It is defined as:

$$RE = \frac{|x_0| - |x|}{|x|} \times 100\ \% \tag{7}$$

where '| |' means the absolute value, x is the 'true' value, x_0 is the influenced value. *RE* > 0 means the exerted influence will cause the measurement value to be larger than 'true' value and vice versa.

3 Results

3.1 Wind measurement evaluation

Evaluation of the wind measurement performance from the UAV-based EC system includes three contents: (1) measurement precision and its ability to resolve the mesoscale variations of the wind, (2) checking the quality of the acquired calibration parameters, and (3) checking whether the measured wind vector is affected by upwash flow and leverage effects.

First, according to the equations described in Supplement Part A (Eqs. S18 to S23), the measurement precision for horizontal wind components is a function of true airspeed and true heading, while, the measurement precision for vertical wind component is largely decided by the true airspeed. The typical values of true airspeed ranging from 25 m s^{-1} to 35 m s^{-1} (interval of 1 m s^{-1}) and the true heading values ranging from 0° to 180° (interval of 30°) were used in the evaluation of wind measurement error. Then, the measurement precision (1σ) of the geo-reference 3D wind vector from aircraft was estimated using the measurement precision of the related parameters from Table 1. The results are shown in Figure 4 for the measurement precision of horizontal wind (σ_u and σ_v in Figs. 4a and 4b) and vertical wind (σ_w in Fig 4c), respectively. The typical values of the measurement precision are ranging from 0.05 m s^{-1} to 0.07 m s^{-1} for horizontal wind component u, ranging from 0.02 m s^{-1} to 0.08 m s^{-1} for horizontal wind component v, and ranging from 0.05 m s^{-1} to 0.07 m s^{-1} for vertical wind component w. When the flight direction is towards due east or due west, the horizontal wind (u and v) has the smallest measurement error.

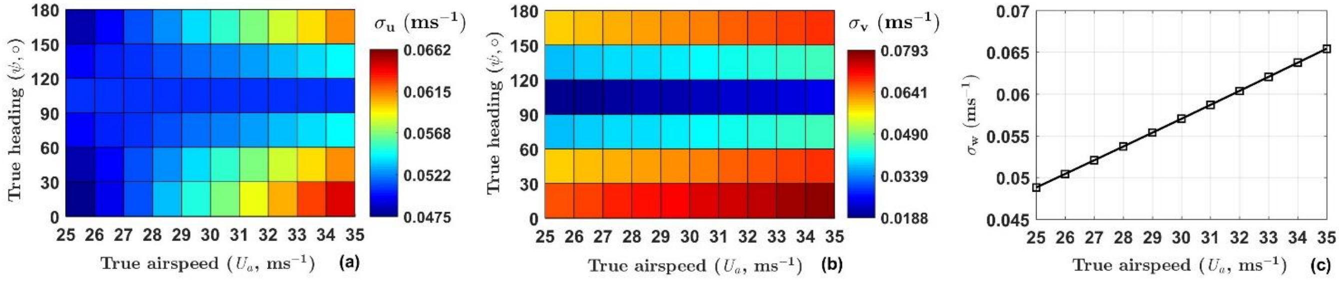

Figure 4. Estimated measurement precision (1σ) of the horizontal wind (a, b) and vertical wind (c) according to the equations described in Supplement Part A (Eqs. S18 to S23).

Generally speaking, an autopiloted UAV can maintain a near-constant true airspeed during the cruise flight phase. For a true airspeed of 30 m s^{-1} for the current UAV-based EC system during the cruising, the maximum measurement error in the northward, eastward, and vertical velocities of the geo-referenced wind components were calculated as approximately 0.06, 0.07, and 0.06 m s^{-1}, respectively. Then, we assume that a minimum signal-to-noise ratio of 10:1 is required to measure the wind components with sufficient precision for EC measurements (Metzger et al., 2012). Accordingly, in the real environments, horizontal and vertical wind speed greater than 0.7 m s^{-1} and 0.6 m s^{-1} can be reliably measured, respectively (Table 2).

Table 2: The maximum measurement error in the northward (u), eastward (v), and vertical (w) velocities of the geo-referenced wind components at the true airspeed of 30 m s^{-1}, and the least resolvable magnitude assuming the minimum required signal-to-noise ratio of 10:1.

Measurements	Measurement precision (1σ)	Least resolvable magnitude
u-windspeed (m s^{-1})	0.06	0.6
v-windspeed (m s^{-1})	0.07	0.7
w-windspeed (m s^{-1})	0.06	0.6

The above results gave the nominal precision for wind measurements that does not consider the influence of environmental conditions. Changes in the environment will lead to sensor drift, increasingly deteriorating the measurement with flight duration (Metzger et al., 2012; Lenschow and Sun, 2007). Following the methods of Lenschow and Sun (2007), the ability of the limitations of the accuracy of wind field measurements from UAV to resolve the mesoscale variations of the 3D wind components in the encountered atmospheric conditions was assessed. For the vertical wind, the mesoscale variability was defined as the peak signal magnitude of the power spectra curve. The corresponding average wavenumber was determined as 0.09 m^{-1} based on the straight flight leg (about 4 km, lasting about 120 s) of the standard operational flight. Then, the minimum required signal level for the vertical wind measurement was estimated as $\partial w/\partial t \simeq 0.14$ m s^{-2}. The accuracy of the vertical wind measurement using Eq. (2) is estimated as follows. The first term on the right-hand side of Eq. (2) is dominated by the drift in the differential pressure transducer, the value of $\partial U_a = 0.05$ m s^{-1} acquired from the wind tunnel test was applied (Table 1). The histogram of Θ derived from the standard operational flights is shown in Figure 5. The 99 % confidence interval indicates that the value of Θ seldom exceeds $\pm 3°$, i.e., ± 0.053 radians. Thus, the value of the first term was estimated as 2.2×10^{-5} m s^{-2}.

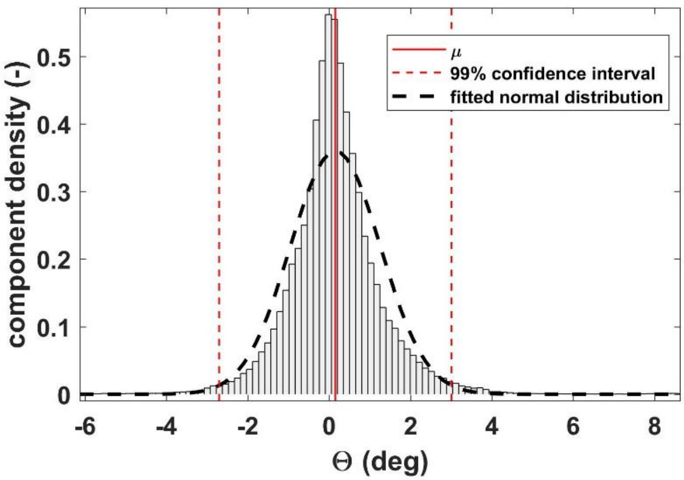

Figure 5. Histogram of Θ derived from the standard operational flight. Component density is scaled so that the histogram has a total area of one. Red vertical lines indicate distribution average (solid) and 99% confidence interval (dashed). The black dashed bell curve displays a reference fitted normal distribution.

The second term in Eq. (2) is a combination of INS pitch accuracy and drift in the measured attack angles. The combined accuracies of these two sensors were applied to derive $\partial\Theta = 0.0024$ radians. Thus, the second term in Eq. (2) was estimated as 6×10^{-4} m s^{-2}. Finally, the third term in Eq. (2) was estimated as 1.7×10^{-4} m s^{-2}, according to the stated accuracy of the vertical velocity from the INS. The overall performance of the vertical wind measurement (7.9×10^{-4} m s^{-2}) was accurate enough to resolve the mesoscale variations in vertical air velocity.

The required accuracy of horizontal wind for mesoscale measurement was estimated as 10 times larger than that of vertical wind, i.e., $\partial u/\partial t \simeq \partial v/\partial t \simeq 1.4$ m s^{-2}. The measurement accuracy of the horizontal wind component u was estimated as 4.8×10^{-4} m s^{-2} according to Eq. (3). Like the first term in Eq. (2), with the value of Ψ rarely exceeding ± 0.18 radians, the measurement accuracy of the horizontal wind component v was estimated as 2.7×10^{-2} m s^{-2}according to Eq. (4). Thus, the measurement accuracy of the horizontal wind components was accurate enough to resolve the mesoscale variations in the horizontal air velocity as well.

Second, before checking the quality of the acquired calibration parameters, the calibration results of the offset in pitch (ϵ_θ) and heading (ϵ_ψ) angles based on the ‘box’ maneuver are provided in Supplement Part C (Figs. S2 and S3). The final calibration values are $\epsilon_\theta = -0.183°$ and $\epsilon_\psi = 2°$. In order to verify the quality of these calibration parameters, a ‘racetrack’ maneuver was performed. Figure 6 shows the verification results by plotting wind vector and calculating summary statistics for the ‘racetrack’ maneuver (including turns), using the initial ($\epsilon_\theta = \epsilon_\psi = 0°$, Fig. 6a) and calibrated (Fig. 6b) set of parameters. The introduction of the calibration parameter effectively improved the quality of geo-referenced wind vector measurement. The standard deviation for wind direction, $\sigma_{U_{dir}}$, is 4.9° for the calibrated set compared to 8.7° for the initial set, and the standard deviation of wind speed, σ_U, is 0.52 m s^{-1} for the calibrated set compared to 1.12 m s^{-1} for the initial set. The average vertical wind speed is much closer to zero ($\overline{w} = -0.006 \text{ m s}^{-1}$) for the calibrated set than for the initial set ($\overline{w} = 0.1 \text{ m s}^{-1}$). For the horizontal wind, it is evident from Fig. 6 that the wind direction and velocity are little affected by sharp turns. On the contrary, the measurement of the vertical wind component is obviously affected by turns in flight, as shown by the large ripple in the vertical wind speed around the scan value of 150 (Fig. 6). It should be noted that the influence of upwash flow and the leverage effect are not considered in the calculated of geo-referenced wind vector.

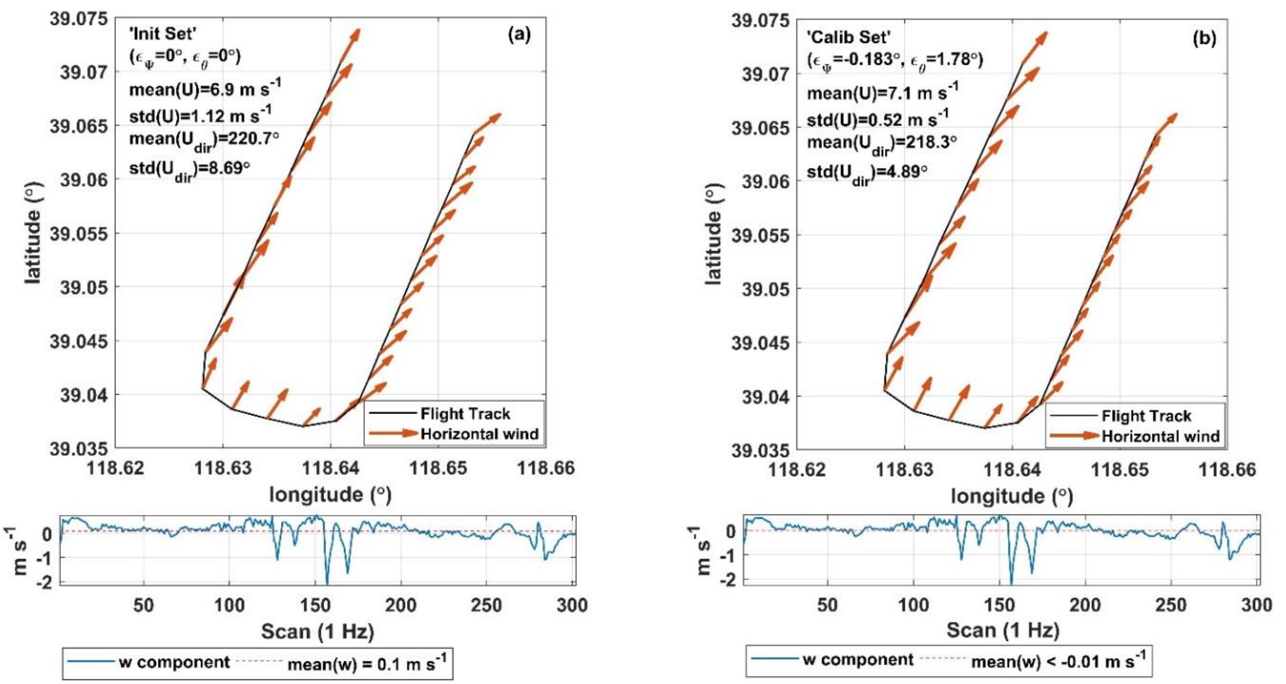

Figure 6. Quality check of the calibration parameter by plotting wind vector and calculating summary statistics for the ‘racetrack’ maneuver, using the initial (a) and calibrated (b) set of parameters. The calibration flight was carried out on 4 September 2022 at the Caofeidian Shoal Harbor.

Third, in order to check the influence of the lift-induced upwash on the attack angle measurement from the 5HP, an ‘acceleration-deceleration’ flight maneuver was performed. During the ‘acceleration-deceleration’ maneuver, INS data shown a vertical velocity of the UAV at 0.05±0.2 m s^{-1}, the altitude of UAV at 392±0.6 m, the heading of UAV at 199±2.4°. The flight conditions met the requirements of the ‘acceleration-deceleration’ maneuver (Vellinga et al., 2013). The relationship between the pitch angle (θ) measured by INS and the attack angle (α) measured by 5HP is plotted in Figure 7, where the attack angle was not corrected for lift-induced upwash. The slope (0.94) between θ and α is close to its theoretical value of 1, and the intercept (0.16) is close to zero. This result indicates that the lift-induced upwash has only a very small effect on the attack angle, and the influence of upwash could be ignored.

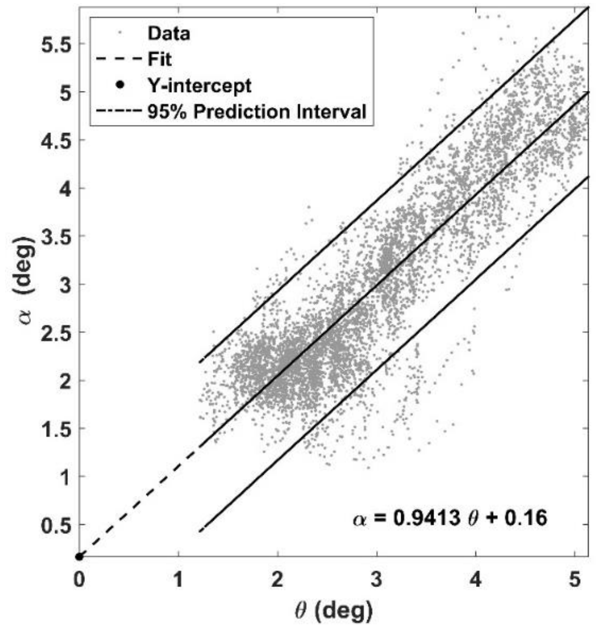

Figure 7. Relationship between the pitch angle (θ) measured by INS and the attack angle (α) measured by 5HP. The fitted linear equation is also shown.

Finally, the geo-referenced wind vector was calculated with and without the correction for the leverage effect based on the measurement data from the 'acceleration-deceleration' flight maneuver. The average relative differences between the corrected and uncorrected horizontal and vertical wind speeds are 0.1 % and 0.2 %, respectively. The standard deviation for horizontal wind speed is 0.307 m s^{-1} without the level arm term compared to 0.306 m s^{-1} when the level arm term is introduced. The standard deviation of vertical wind speed is 0.254 m s^{-1} without the level arm term compared to 0.253 m s^{-1} with the level arm term. The correction of leverage effect had minimal effect on improving the geo-referenced wind vector measurement; therefore, this correction term can be ignored.

3.2 Flux measurement error caused by instrumental noise

Flux measurement error caused by the instrumental noise gives the lowest limit of the flux that the UAV-based EC system is able to measure. Such measurement error was assessed by combining the covariance uncertainty estimated by RS method and the propagation of errors in flux correction terms. Before estimating the flux covariance uncertainty using RS method, using the measured data from each straight and level flight leg of the standard operational flight (Fig. 2), the normalized integrated cospectra (ogives) curves of sensible heat (Fig. 8a), latent heat (Fig. 8b), and CO_2 (Fig. 8c) flux are formed as a function of wavenumber (k), where $k = 2\pi f / U_a$. As shown in Figure 8, although the heterogeneous turbulence (or mesoscale turbulence) interfered the shape of ogive curves, most curves converged at the high and low frequency ends, which indicated that these segmented data were sufficiently long to represent the lowest significant frequencies contributing to the covariance.

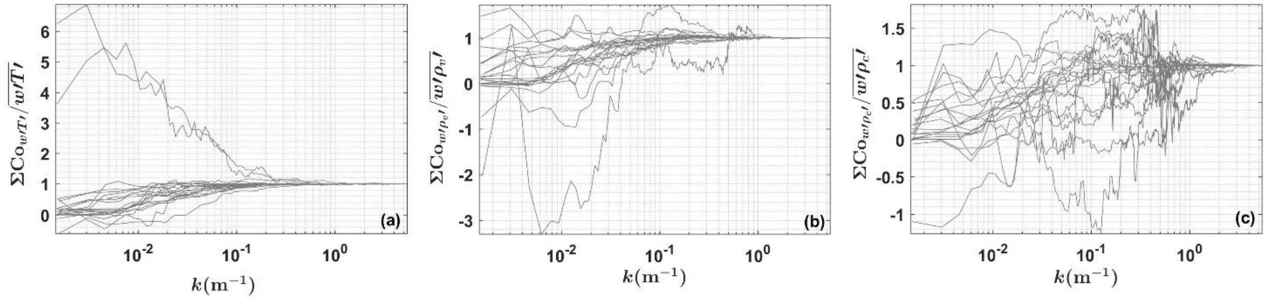

Figure 8. Normalized ogive curves as a function of wavenumber for the flux covariance of sensible heat (a), latent heat (b), and CO_2 (c) from each straight and level flight leg of the standard operational flight in Section 2.2.2.

Then, the results of instrumental noise related relative flux measurement error compared to the magnitude of the flux are shown in Figure 9. It can be seen that the flux measurement error caused by instrumental noise significantly decreases when the flux magnitude increases. It is not surprising since, in theory, instrumental noise is usually close to a constant and the relative flux measurement error caused by instrumental noise will decreases with increasing measurement magnitude. Overall, instrumental noise has the least effect on latent heat flux (ranging from 0.02% to 2.42% in this study) measurements, followed by sensible heat flux (ranging from 0.05% to 8.6% in this study), and has the greatest effect on the measurement of CO_2 flux (ranging from 0.22% to 75.6% in this study). Then, a simple rational function relationship between the relative measurement error and the flux magnitude is fitted according to the measured data, where the constant term in the denominator is set to 0. The fitted coefficient in the numerator can be considered as the flux measurement error caused by instrumental noises, which are 0.03 μmol m^{-2} s^{-1}, 0.02 W m^{-2}, and 0.08 W m^{-2} for the measurement of CO_2 flux, sensible and latent heat flux, respectively. At last, using the signal-to-noise ratio of 10:1, the minimum magnitudes for reliably resolving the CO_2 flux, sensible and latent heat fluxes were estimated as 0.3 μmol m^{-2} s^{-1}, 0.2 W m^{-2}, and 0.8 W m^{-2}, respectively.

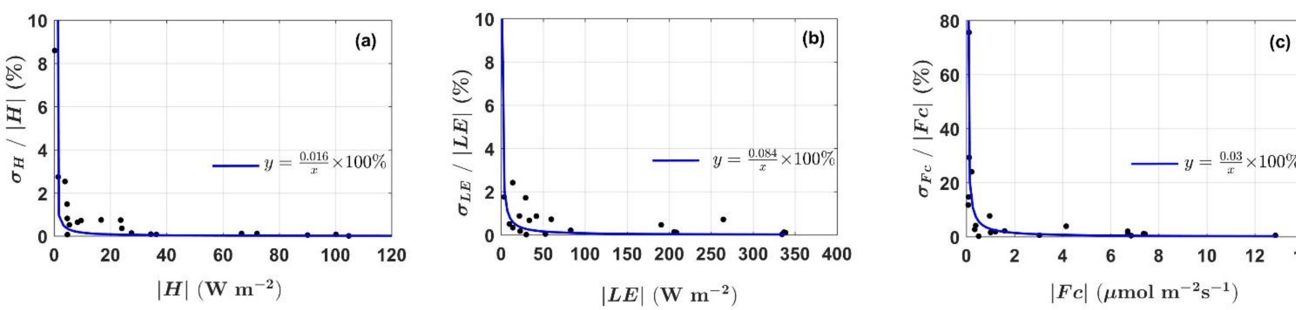

Figure 9. Relative flux measurement error caused by instrumental noise plotted against the magnitude of the flux. Also shown the fitted error curves. Measured data was from the standard operation flights in Section 2.2.2.

3.3 Resonance noise

The resonance noise from the engine and propeller can lead to systematic overestimation of the variance and covariance of the observed atmospheric scalars. Since the noise mainly appears in the high frequency domain of the (co)spectra, the reference (co)spectral curve of Massman and Clement (2005) was used to quantify the systematically bias caused by the resonance noise.

All spectra curves of the variance of measured scalars (including air temperature, H_2O, and CO_2 concentration) approximately followed the reference spectra curve and the reference -2/3 slope in the inertial subrange (Figs. 3a to 3c). The largest scatter occurred in the spectra of CO_2 (Fig. 3c). When comparing the spectra curve with the reference spectra, the resonance noise led to a systematic deviation in the variance of air temperature, H_2O, and CO_2 concentration of 0.1±0.1 %, 1.0±0.79 %, and 4.4±0.66 %, respectively, relative to the entire frequency range. For the flux covariance of sensible, latent heat and CO_2, all the co-spectra curves approximately follow the reference co-spectra curve and the reference -4/3 slope in the inertial subrange (Figs. 3d to 3f). Compared with the reference co-spectra, the resonance noise led to a systematic deviation in the flux of sensible, latent heat, and CO_2 of 0.07±0.004 %,0.3±0.25 %, and 2.9±1.62 %, respectively, relative to the entire frequency range.

The results show that the resonance noise has a very little impact on the measured variance and flux covariance. Among them, the measurements of CO_2 concentration and flux are most susceptible to the resonance noise, but the impact of this noise is limited to around 5 % of the observed value.

3.4 Sensitivity analysis

In this study, in order to investigate the relevance of the calibration parameters for the measurement of the geo-referenced wind vector and turbulent flux, two sensitivity tests were conducted by adding an error of ± 30 % to the used optimum parameters ($\epsilon_\psi, \epsilon_\theta, \epsilon_\phi, \epsilon_r$). We assumed that the maximum uncertainties contained in the calibration parameter is not more than 30 % of its own value.

First, the sensitivity of the geo-referenced 3D wind and turbulent flux to the uncertainty in the individual parameter was tested. The *RE* value is used to quantify the sensitivity, and the results are summarized in Tables 3 and 4. For the measurement of the geo-referenced wind vector, Table 3 shows that the uncertainties in the temperature recovery factor (ε_r) and 5HP mounting misalignment error in the roll (ϵ_ϕ) angle do not contribute significantly to errors in the wind measurements, which were typically smaller than 4% of the observed value in this study. Parameter ε_θ had the largest effect on the vertical wind component (up to 30 %), whereas ε_ψ had the largest effect on the horizontal wind component. For the measurement of turbulent fluxes, Table 4 shows that the errors in ε_r and ϵ_ϕ does not significantly influence the flux measurements, typically small than 5% of the observed value in this study. The uncertainties in calibration parameter ε_θ and ε_ψ had significant effects on the measurement of turbulent flux. Adding an error of ± 30 % to ε_θ result in significant perturbation (large *RE* variance) in the measured turbulent fluxes including sensible heat, latent heat and CO_2. While, errors in ε_ψ to some extent mainly affect the measurement of latent heat flux (*RE* may up to 15 %).

Table 3: *RE* of the sensitivity test for the geo-referenced 3D wind vector (u, v, w). An error factor of ±30 % was added to each calibrated parameter. The geo-referenced 3D wind vector was calculated based on the straight leg of the standard operational flight.

Parameter	Error (%)	*RE* of geo-referenced 3D wind vector mean ± std		
		u (%)	v (%)	w (%)
$\boldsymbol{\varepsilon_r}$	-30	0.04 ± 0.41	-0.004 ± 2	0 ± 0
	30	0.06 ± 0.43	0.27 ± 1.1	-0.07 ± 0.23
$\boldsymbol{\varepsilon_\varphi}$*	-30	0.41±2.51	-0.09±2.05	1.15±2.43
	30	-0.43±2.61	0.09±1.79	-1.1±2.66
$\boldsymbol{\varepsilon_\theta}$	-30	0.03±0.41	-0.35±2.54	-30.51±6.42
	30	0.05±0.45	0.42±1.82	30.37±6.61
$\boldsymbol{\varepsilon_\psi}$	-30	2.98±25.06	-2.04±16.3	0±0
	30	-2.97±24.96	2.42±16.63	0±0

* The optimum calibration value is set to 0, ε_φ was varied over $\pm0.9°$, which is 30 % of its typical range.

Table 4: *RE* of the sensitivity test for the turbulent fluxes. An error factor of ±30 % was added to each calibrated parameter. The turbulent fluxes were calculated based on the straight leg of the standard operational flight.

Parameter	Error (%)	*RE* of turbulent flux mean ± std			
		Fc (%)	*H* (%)	LE (%)	u* (%)
$\boldsymbol{\varepsilon_r}$	-30	1.04±3.04	-0.76±4.82	0.1±0.29	0±0
	30	-1.0±3.3	0.74±4.8	-0.1±0.29	0.2±1.07
$\boldsymbol{\varepsilon_\varphi}$*	-30	0.07±1.2	0.03±0.7	0.15±1.51	0.54±1.71
	30	-0.14±0.89	-0.06±0.7	-0.16±1.46	0.12±1.61
$\boldsymbol{\varepsilon_\theta}$	-30	-3.27±11.18	-0.8±9.48	0.19±11.91	-4.08±5.61
	30	2.34±10.52	-0.44±8.24	-1.27±9.92	3.73±4.53
$\boldsymbol{\varepsilon_\psi}$	-30	1.78±5.18	-0.73±4.87	1.89±13.42	0.63±5.75
	30	-0.99±3.96	-0.57±3.26	2.66±11.76	-0.59±4.42

* See Table 3.

The second sensitivity test was performed to evaluate the overall interaction between calibration parameters and the calculation of geo-referenced wind vector and turbulent flux by adding an error of ±30 % to all the calibration members simultaneously. Tables 5 and 6 provided a summary of the *RE* results from the second sensitivity test. For the measurement of geo-referenced wind vector (Table 5), adding an error of ±30 % to all the calibration parameters at the same time resulted in great perturbations to both the horizontal (low *RE* with high variance) and vertical wind components (high *RE* with low variance). For the measurement of turbulent fluxes, 30% error in the calibration parameters can result in errors in measured fluxes more than 10%. In addition, Table 6 reveals that the latent heat flux is more sensitivity to the errors in the calibration parameter than other flux measurement (higher mean and variance of the *RE* compared to other measurements).

Table 5: *RE* of the sensitivity test for the geo-referenced 3D wind vector (u, v, w) calculated by adding an error of ± 30 % to all the calibrated parameter simultaneously. The geo-referenced 3D wind vector was calculated based on the straight leg of the standard operational flight.

Parameter	Error (%)	*RE* of geo-referenced 3D wind vector mean ± std		
		u (%)	v (%)	w (%)
All	-30	4.24±27.89	-3.2±21.1	-29.35±4.63
	30	-4.15±27.46	3.55±21.91	29.16±4.86

Table 6: *RE* of the sensitivity test for the turbulent flux calculated by adding an error of ± 30 % to all the calibrated parameter simultaneously. The turbulent flux was calculated based on the straight flight leg of the standard operational flight.

Parameter	Error (%)	*RE* of turbulent flux mean ± std			
		Fc (%)	*H* (%)	LE (%)	u* (%)
All	-30	-1.19±10.51	-0.9±8.06	2.71±13.91	-2.92±8.19
	30	-0.49±10.01	-1.66±5.4	-6.07±13.24	1.74±6.55

4 Discussions

As one in a new generation of airborne flux measurement platforms, the UAV-based EC system can significantly reduce the cost of implementing airborne flux measurement campaigns and greatly promote their wide application at regional scales. The current study aimed to evaluate the basic performance of the UAV-based EC system developed by Sun et al. (2021a) in the measurement of wind vector and turbulent flux.

First, the wind measurement precision (nominal precision) of the UAV-based EC system was estimated by propagating the sensor errors to the geo-referenced wind vector using the linearized Taylor series expansions from Enriquez and Friehe (1995) . The 1σ precision of geo-referenced wind measurement was estimated to be ± 0.07 m s^{-1}, and the least resolvable magnitude for wind measurement was estimated at 0.7 m s^{-1} by assuming the minimum signal-to-noise ratio of 10:1. The derived wind measurement minimum resolvable magnitude can be used as a basic reference for wind measurement capability of the UAV-based EC system, and the measured values of wind vector smaller than the minimum resolvable values should be considered unreliable. The accuracy of the sensors was also assessed by examining the collected data in the real environment (Lenschow and Sun, 2007; Thomas et al., 2012). Our results revealed that the overall performance of geo-referenced wind measurement is sufficient accuracy for resolving the mesoscale variations of the 3D wind components under the encountered atmospheric conditions. Therefore, it is possible to capture the mesoscale variability of the atmospheric boundary layer (ABL) over a wide range of spatial scales by performing longer flight paths.

Second, based on the measurement data from the in-flight calibration campaign, several key factors affecting the accuracy of geo-referenced wind measurement were analysed. First, the UAV-based EC system was calibrated (in Supplement Part C) using measured data from the 'box' flight maneuver to correct the mounting misalignment between the 5HP and the CG of the

UAV in the heading ($\epsilon_\theta = -0.183°$) and pitch ($\epsilon_\psi = 2°$) angles. The quality of the acquired calibration parameters was verified using the 'racetrack' flight maneuver, and the acquired calibration value effectively improved the observed wind field with smaller variance compared with the wind calculated using their initial value. At the same time, the measurement of the vertical wind component was significantly affected by the in-flight turn (maintaining about 20° roll). Therefore, it is necessary to avoid using the measured data from the turn section for turbulent flux calculation. Compared to other studies (Vellinga et al., 2013; Reineman et al., 2013), the relatively large variance in the horizontal wind and wind direction after calibrated in this study may be caused by the nonstationary condition of the turbulence. This was caused by the reason that the flight altitude of 400 m was not high enough to totally avoid interaction from the underlying surface.

The current calibration procedure did not include methods to determine the offset angle in roll (ε_φ) and the temperature recovery factor (ε_r) because of the small vertical separation (27.3 cm) between the 5HP and the roll axis of the UAV and the small Mach number (<0.1) during operational flight. The default ($\varepsilon_\varphi = 0°$) and empirical ($\varepsilon_r = 0.82$) value were adopted for these two calibration parameters. The sensitivity analysis shown these two parameters have no large effect on the wind vector and turbulent flux.

It should be noted that wind measurements from the airborne platform may be susceptible to flow distortion and rigid-body rotation (leverage effects). Generally, the influence of these two factors were ignored by UAV platform when calculating the geo-referenced wind vector. To confirm that these effects could be safely ignored, data from 'acceleration-deceleration' flight maneuver was used to analyse the effects of lift-induced upwash and the leverage effect on the wind measurements. Our results demonstrate that the upwash has almost no effect on the wind measurement, which was indicated by the near 1:1 relationship (0.94 in Fig. 7) between the measured attack angles and pitch angle. The slight departures from the ideal 1:1 relationship may have been caused by the nonstationary condition during the flight. For the influence from the leverage effects, the differences in 3D wind vector between corrected and uncorrected for the leverage effect is very small. Thus, ignoring the influence of the leverage effect has almost no effect on the measurement of wind. Therefore, we concluded that the geo-referenced 3D wind vector can be measured reliably by the current UAV-based EC system without considering the interference from the lift-induced upwash and leverage effects.

Third, instrumental noise related relative flux measurement error was estimated by combining the covariance uncertainty estimated by RS method and the propagation of errors in flux correction terms. By assuming that the instrumental noise is close to a constant, we fitted a simple rational function relationship between the relative measurement error and the flux magnitude according to measured data (Fig. 9), and the fitted coefficient in the numerator can be considered as the flux measurement error caused by instrumental noises. The estimated flux measurement error of CO_2, sensible and latent heat flux are 0.03 μmol m^{-2} s^{-1}, 0.02 W m^{-2}, and 0.08 W m^{-2}, respectively. Since the RS method directly uses the shuffled raw measurement data to calculate the instrumental noise induced flux measurement error, its estimated results inevitably included the effects of resonance noise from the UAV. Using the signal-to-noise ratio of 10:1, the least resolvable magnitude for turbulent flux measurement was estimated to be 0.3 μmol m^{-2} s^{-1} for the CO_2 flux, 0.2 W m^{-2} for the sensible heat flux, 0.8 W m^{-2} for the latent heat flux, respectively.

Fourth, because the UAV-based EC system has not completely insulated the noise from the operation of the engine and propeller and its effect on the measured scalars, the reference (co)spectra of Massman and Clement (2005) was used to quantify the effect of the resonance noise on the variance and flux of the measured scalars. Previous studies found that the influence of resonance noise mainly appears in the high frequency domain of the power spectra of the measured atmospheric scalars (e.g., air temperature, H_2O, and CO_2 concentration). The frequency range of the noise region was artificially designated for air temperature, water vapor and CO_2. By calculating the area difference of the designated frequency range beneath the (co)spectral curve between the measured and reference (co)spectral curves, the resonance effect could be quantified. The results shown that, overall, resonance noise has little impact on the variance and flux covariance of the measured scalars. The measurements of CO_2 concentration and its flux covariance were the most susceptible to resonance noise, but the maximum effect was less than 5 %. It should be noted that this method may overestimate the deviation caused by resonance noise as indicated by the reference (co)spectra curve and the measured (co)spectra not fully overlapping in the inertial subrange (shown in Fig. 3).

In general, gas detection based on optical absorption methods can achieve fast and high precision gas concentration measurements, but they are extremely sensitive to vibration noise. However, due to the limited space inside the UAV, it is difficult to install all the hardware needed for a complex vibration isolation structure to effectively isolate the impact of vibration on the gas analyser. The weight and the aerodynamic shape of the UAV also present challenges. In the future, a new UAV-based EC system based on a pure electric UAV will be developed. The electro-powered UAV has similar performance to the current fuel-powered UAV but can minimize the impact of vibration noise from the engine and propeller rotation, which makes it possible to completely isolate the resonance effect using a simple vibration isolation structure. Electro-powered UAVs also have other advantages including larger wingspan (lower cruising speed), a constant CG position, and lower operational complexity compared to the current system.

Fifth, two sensitivity tests were conducted to assess the perturbation of the geo-referenced wind velocity and turbulent flux under variation (± 30 %) of each calibration parameter around its optimum value ($\epsilon_\psi = 2°, \epsilon_\theta = -0.183°, \epsilon_\phi = 0°, \epsilon_r = 0.82$) as well as under simultaneous variation (± 30 %) of all calibration parameters. Their *RE* was used to evaluate the sensitivity, and values of wind and flux less than their least resolvable magnitude were removed from the calculation. The results revealed that uncertainties in the temperature recovery factor (ε_r) and mounting offset in roll angle (ε_φ) do not significantly contribute to an error in the measurement of wind vector and turbulent fluxes. The typical *RE* for the geo-referenced wind measurements is less than 1.2 % with variance less than 3 %, and the typical *RE* for turbulent flux is less than 1.1 % with variance less than 5 %. Calibration parameters that had the largest effect on the measurement of geo-referenced wind vector and turbulent flux are the mounting offset angle in pitch (ε_θ) and heading (ε_ψ). Uncertainties in ε_θ had a direct effect on the measurement of vertical wind component, and then these errors propagate to the measured fluxes, resulting in a large error contains in the measured fluxes (~15 %). A negative error in ε_θ will lead to an underestimation of the vertical wind and vice versa. Errors in ε_ψ directly affect the measurement of the horizontal wind, and to some extent, the measurement of turbulent flux. The difference is that the added error in ε_ψ lead to a great variability (up to 25 %) in the *RE* of horizontal wind. By checking the relationship between the magnitude of the horizontal wind (u, v) and *RE*, a near exponential relationships was seen, as shown in Figure 10. The influence of the error in the ε_ψ decreased significantly with the increase in the magnitude of the horizontal wind velocity. Additionally, the measurement of latent heat flux may be greatly affected by the error in ε_ψ, which is reflected by the relatively large deviancy (~14 %) of the *RE*. Therefore, calibration parameter ε_θ and ε_ψ need to be carefully calibrated.

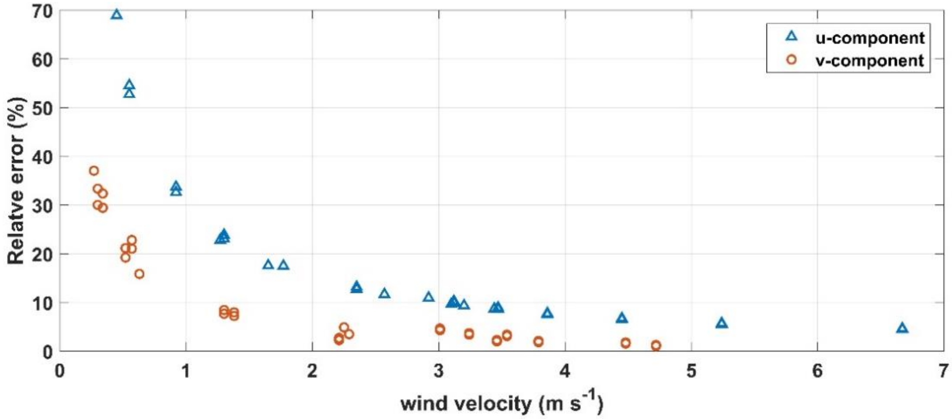

Figure 10. Relationship between the magnitude of the horizontal wind velocity (u, v) and *RE* from the sensitivity test.

Lastly, it should be noted that the accuracy of the measured geo-referenced wind vector and turbulent flux from the UAV-based EC system is subject to the combination of many factors, mainly including sensor accuracy, UAV powerplant, UAV fluctuation (e.g., variation of the UAV attitude and flight height), and the atmospheric conditions during the measurements, etc. This study mainly focused on assessing the effects of sensor precision and UAV powerplant on the measurement errors of geo-referenced wind vector and turbulent flux. Evaluation results gave the lowest limit of the wind vector and turbulent flux that the UAV-based EC system can measure. Another effective way to evaluate the measurement accuracy of this new technique is by comparing measured values with those from the traditionally recognized measurement. However, the direct comparison of flux measurements between aircraft and traditional ground tower is still challenging due to the difference in the measurement height, mechanism (time series for ground EC and space series for aircraft), and instruments (e.g., wind sensor). Previous studies have extensively compared the measurement of fluxes and wind vector between airborne and ground-based EC methods and found consistent results (Gioli et al., 2004; Metzger et al., 2012; Sun et al., 2021b). At the same time, substantial and consistent over- or underestimation of the measured wind and fluxes by UAV compared to ground measurements were observed and reported. These differences may be due to several factors such as vertical flux divergence (the measurement height of UAV is higher than ground-tower), surface heterogeneity (induced by the larger footprint region of the UAV compared to the ground tower), measurement errors (e.g., window length, resonance noise, etc.) as well as their difference in platform and sensors. Therefore, it is necessary to conduct a comparison test on the same platform and under the same environment to exclude the influence of these factors. Inspired by Reineman et al. (2013), future work can include developing a ground-vehicle-based UAV flux validation platform. This platform could carry both the UAV-based and traditional ground EC system to assess the measurement accuracy of the UAV-based EC system with the measurement of ground EC as the benchmark in a flight-like scenario.

5 Conclusions and further works

The main objective of this study was to quantitatively evaluate the performance of the developed UAV-based EC system in the measurement of geo-referenced wind vector and turbulent flux. In terms of measuring precision, turbulence measurements from the UAV-based EC system were achieved with sufficient precision to enable reliable measurement of geo-referenced wind and EC flux. Magnitudes larger than 0.7 m s^{-1} for wind velocity, 0.3 μmol m^{-2} s^{-1} for CO_2 flux, 0.2 W m^{-2} for sensible heat flux, and 0.8 W m^{-2} for latent heat flux could be reliably measured by the UAV-based EC system by assuming the minimum required signal-to-noise ratio of 10:1 for EC application. Based on the data from the calibration flight, the carefully calibrated offset angle in pitch (ϵ_θ) and heading (ϵ_ψ) were shown to effectively improve the quality of wind field measurements, and the influences of flow distortion and the leverage effect on the wind measurement were minimal and could be ignored. The influence of resonance noise was small on the measurement of air temperature and water vapor (typically < 1 % for their variance and flux covariance), but relatively large on the measurement of CO_2 (around 5 % for variance and flux covariance).

The relevance of the calibration parameters ($\varepsilon_r, \epsilon_\phi, \varepsilon_\psi, \varepsilon_\theta$) for the measurement of the geo-referenced wind vector and turbulent flux was also assessed based on two sensitivity tests. The measurements of the geo-referenced wind vector and turbulent flux were insensitive to the errors in the ε_r and ϵ_ϕ. Uncertainties in the calibration parameter ε_θ and ε_ψ had the strongest effects on the measurements. Because of ε_θ directly determining the magnitude of the vertical wind, its error will lead to uncertainties in vertical wind measurement and then propagate the uncertainties to the measurement of turbulent flux. The uncertainties in ε_ψ have a direct effect on the measurement of horizontal wind, and to some extent, the measurement of turbulent flux. Therefore, these two calibration parameters need to be carefully calibrated. Conducting the UAV-based EC measurement when wind velocity is larger than 2 m s^{-1} can led to more stable and reliable (*RE* < 20%) results of the wind speed measurement compared to a relatively windless environmental.

Finally, we concluded that the developed UAV-based EC system measured the geo-referenced wind vector and turbulent flux with sufficient precision. The lift-induced upwash and leverage effect had almost no effect on the measurement of geo-referenced wind vector. The resonance effect caused by the operation of engine and propeller mainly affected the measurement of CO_2, and its effect on variance and flux covariance was around 5 %. The quality of calibration parameters ε_ψ and ε_θ has a significant effect on the measurement of the geo-referenced wind vector and turbulent flux, underscoring the importance of careful calibration. Although UAV-based EC measurements have many advantages over manned aircraft and tower-based EC measurements, airborne EC measurements themselves have some shortcomings, such as flux results hard to interpret (e.g., influence from surface heterogeneity, flux divergence, etc.), the measurements are restricted to short periods of time, and the interaction between the UAV and turbulence. Future researches may include the development of a new generation UAV-based EC system with the following improvements: 1) a new electro-powered UAV platform with the advantages of being quieter (low noise), having a low cruising speed, and being easy to operate; 2) a ground-vehicle-based validation platform to enable direct comparative evaluation of the UAV-based EC system with traditional ground EC methods under near-identical environmental conditions; 3) a graphics based real-time monitoring system to make it possible to change the flight pattern according to real-time data; and 4) a number of integrated field observation experiments that combining ground-based EC networks, OMS, and multi-source satellite RS to further prompt the development of theory and methodology for scaling transformation. Ultimately, the versatility of the UAV-based EC system as a low cost and widely applicable environmental research aircraft facilitates further improving our understanding of the energy and matter cycling processes at regional scales.

Author contributions. SY, GB and LX planned the field campaign; SY, LB, JJ, ZZ and JS carried out the field measurements. SY, LS and XZ analysed the data and wrote the manuscript draft. SB, and QZ reviewed and edited the manuscript.

Competing interests. The authors declare that they have no conflict of interest.

Acknowledgments. This work was supported by the National Natural Science Foundation of China (Grant No. 42101477). We would like to thank F-EYE UAV Technology Co. Ltd. for building, maintaining, and operating the UAV in this study.

Data availability. Data for this research are not publicly available due to its proprietary nature currently. The UAV calibration flight data and the standard operation flight data in this study are available upon request to the corresponding author.

References

Anderson, K. and Gaston, K. J.: Lightweight unmanned aerial vehicles will revolutionize spatial ecology, Frontiers in Ecology and the Environment, 11, 138-146, https://doi.org/10.1890/120150, 2013.

Bange, J. and Roth, R.: Helicopter-Borne Flux Measurements in the Nocturnal Boundary Layer Over Land – a Case Study, Boundary-Layer Meteorology, 92, 295-325, 10.1023/A:1002078712313, 1999.

Båserud, L., Reuder, J., Jonassen, M. O., Kral, S. T., Paskyabi, M. B., and Lothon, M.: Proof of concept for turbulence measurements with the RPAS SUMO during the BLLAST campaign, Atmos. Meas. Tech., 9, 4901-4913, 10.5194/amt-9-4901-2016, 2016.

Billesbach, D. P.: Estimating uncertainties in individual eddy covariance flux measurements: A comparison of methods and a proposed new method, Agricultural and Forest Meteorology, 151, 394-405, https://doi.org/10.1016/j.agrformet.2010.12.001, 2011.

Chandra, N., Patra, P. K., Niwa, Y., Ito, A., Iida, Y., Goto, D., Morimoto, S., Kondo, M., Takigawa, M., Hajima, T., and Watanabe, M.: Estimated regional CO2 flux and uncertainty based on an ensemble of atmospheric CO2 inversions, Atmos. Chem. Phys., 22, 9215-9243, 10.5194/acp-22-9215-2022, 2022.

Chen, J. M., Leblanc, S. G., Cihlar, J., Desjardins, R. L., and MacPherson, J. I.: Extending aircraft- and tower-based CO2 flux measurements to a boreal region using a Landsat thematic mapper land cover map, Journal of Geophysical Research: Atmospheres, 104, 16859-16877, https://doi.org/10.1029/1999JD900129, 1999.

Chen, W., Wang, D., Huang, Y., Chen, L., Zhang, L., Wei, X., Sang, M., Wang, F., Liu, J., and Hu, B.: Monitoring and analysis of coastal reclamation from 1995–2015 in Tianjin Binhai New Area, China, Scientific Reports, 7, 3850, 10.1038/s41598-017-04155-0, 2017.

Crawford, T. L. and Dobosy, R. J.: A sensitive fast-response probe to measure turbulence and heat flux from any airplane, Boundary-Layer Meteorology, 59, 257-278, 10.1007/BF00119816, 1992.

Crawford, T. L., Dobosy, R. J., and Dumas, E. J.: Aircraft wind measurement considering lift-induced upwash, Boundary-Layer Meteorology, 80, 79-94, 10.1007/BF00119012, 1996.

Desjardins, R. L., Brach, E. J., Alvo, P., and Schuepp, P. H.: Aircraft Monitoring of Surface Carbon Dioxide Exchange, Science, 216, 733-735, 10.1126/science.216.4547.733, 1982.

Desjardins, R. L., Worth, D. E., MacPherson, J. I., Bastian, M., and Srinivasan, R.: Flux measurements by the NRC Twin Otter atmospheric research aircraft: 1987–2011, Adv. Sci. Res., 13, 43-49, 10.5194/asr-13-43-2016, 2016.

Drüe, C. and Heinemann, G.: A Review and Practical Guide to In-Flight Calibration for Aircraft Turbulence Sensors, Journal of Atmospheric and Oceanic Technology, 30, 2820-2837, 10.1175/JTECH-D-12-00103.1, 2013.

Elston, J., Argrow, B., Stachura, M., Weibel, D., Lawrence, D., and Pope, D.: Overview of Small Fixed-Wing Unmanned Aircraft for Meteorological Sampling, Journal of Atmospheric and Oceanic Technology, 32, 97-115, 10.1175/JTECH-D-13-00236.1, 2015.

Enriquez, A. G. and Friehe, C. A.: Effects of Wind Stress and Wind Stress Curl Variability on Coastal Upwelling, Journal of Physical Oceanography, 25, 1651-1671, https://doi.org/10.1175/1520-0485(1995)025<1651:EOWSAW>2.0.CO;2, 1995.

Finkelstein, P. L. and Sims, P. F.: Sampling error in eddy correlation flux measurements, Journal of Geophysical Research: Atmospheres, 106, 3503-3509, https://doi.org/10.1029/2000JD900731, 2001.

Garman, K. E., Wyss, P., Carlsen, M., Zimmerman, J. R., Stirm, B. H., Carney, T. Q., Santini, R., and Shepson, P. B.: The Contribution of Variability of Lift-induced Upwash to the Uncertainty in Vertical Winds Determined from an Aircraft Platform, Boundary-Layer Meteorology, 126, 461-476, 10.1007/s10546-007-9237-y, 2008.

Garman, K. E., Hill, K. A., Wyss, P., Carlsen, M., Zimmerman, J. R., Stirm, B. H., Carney, T. Q., Santini, R., and Shepson, P. B.: An Airborne and Wind Tunnel Evaluation of a Wind Turbulence Measurement System for Aircraft-Based Flux Measurements, Journal of Atmospheric and Oceanic Technology, 23, 1696-1708, 10.1175/JTECH1940.1, 2006.

Gioli, B., Miglietta, F., Vaccari, F. P., and Zaldei, A.: The Sky Arrow ERA, an innovative airborne platform to monitor mass, momentum and energy exchange of ecosystems, Annals of Geophysics, 49, 109-116, 10.4401/ag-3159, 2006.

Gioli, B., Miglietta, F., De Martino, B., Hutjes, R. W. A., Dolman, H. A. J., Lindroth, A., Schumacher, M., Sanz, M. J., Manca, G., Peressotti, A., and Dumas, E. J.: Comparison between tower and aircraft-based eddy covariance fluxes in five European regions, Agricultural and Forest Meteorology, 127, 1-16, https://doi.org/10.1016/j.agrformet.2004.08.004, 2004.

Hannun, R. A., Wolfe, G. M., Kawa, S. R., Hanisco, T. F., Newman, P. A., Alfieri, J. G., Barrick, J., Clark, K. L., DiGangi, J. P., Diskin, G. S., King, J., Kustas, W. P., Mitra, B., Noormets, A., Nowak, J. B., Thornhill, K. L., and Vargas, R.: Spatial heterogeneity in CO2, CH4, and energy fluxes: insights from airborne eddy covariance measurements over the Mid-Atlantic region, Environmental Research Letters, 15, 035008, 10.1088/1748-9326/ab7391, 2020.

Hu, G. and Jia, L.: Monitoring of Evapotranspiration in a Semi-Arid Inland River Basin by Combining Microwave and Optical Remote Sensing Observations, Remote Sensing, 7, 10.3390/rs70303056, 2015.

Kaimal, J. C., Clifford, S. F., and Lataitis, R. J.: Effect of finite sampling on atmospheric spectra, Boundary-Layer Meteorology, 47, 337-347, 10.1007/BF00122338, 1989.

Kalogiros, J. A. and Wang, Q.: Aerodynamic Effects on Wind Turbulence Measurements with Research Aircraft, Journal of Atmospheric and Oceanic Technology, 19, 1567-1576, 10.1175/1520-0426(2002)019<1567:AEOWTM>2.0.CO;2, 2002.

Khelif, D., Burns, S. P., and Friehe, C. A.: Improved Wind Measurements on Research Aircraft, Journal of Atmospheric and Oceanic Technology, 16, 860-875, 10.1175/1520-0426(1999)016<0860:IWMORA>2.0.CO;2, 1999.

Kirby, S., Dobosy, R., Williamson, D., and Dumas, E.: An aircraft-based data analysis method for discerning individual fluxes in a heterogeneous agricultural landscape, Agricultural and Forest Meteorology, 148, 481-489, https://doi.org/10.1016/j.agrformet.2007.10.011, 2008.

Kowalski, A. S., Serrano-Ortiz, P., Miranda-García, G., and Fratini, G.: Disentangling Turbulent Gas Diffusion from Non-diffusive Transport in the Boundary Layer, Boundary-Layer Meteorology, 179, 347-367, 10.1007/s10546-021-00605-5, 2021.

Lenschow, D. H.: Aircraft Measurements in the Boundary Layer, in: Probing the Atmospheric Boundary Layer, edited by: Lenschow, D. H., American Meteorological Society, Boston, MA, Boston, https://doi.org/10.1007/978-1-944970-14-7_5, 1986.

Lenschow, D. H. and Sun, J.: The spectral composition of fluxes and variances over land and sea out to the mesoscale, Boundary-Layer Meteorology, 125, 63-84, 10.1007/s10546-007-9191-8, 2007.

Lenschow, D. H., Delany, A. C., Stankov, B. B., and Stedman, D. H.: Airborne measurements of the vertical flux of ozone in the boundary layer, Boundary-Layer Meteorology, 19, 249-265, 10.1007/BF00117223, 1980.

Li, X., Liu, S., Xiao, Q., Ma, M., Jin, R., Che, T., Wang, W., Hu, X., Xu, Z., Wen, J., and Wang, L.: A multiscale dataset for understanding complex eco-hydrological processes in a heterogeneous oasis system, Scientific Data, 4, 170083, 10.1038/sdata.2017.83, 2017.

Li, X., Liu, S., Yang, X., Ma, Y., He, X., Xu, Z., Xu, T., Song, L., Zhang, Y., Hu, X., Ju, Q., and Zhang, X.: Upscaling Evapotranspiration from a Single-Site to Satellite Pixel Scale, 10.3390/rs13204072, 2021.

Li, X., Liu, S., Li, H., Ma, Y., Wang, J., Zhang, Y., Xu, Z., Xu, T., Song, L., Yang, X., Lu, Z., Wang, Z., and Guo, Z.: Intercomparison of Six Upscaling Evapotranspiration Methods: From Site to the Satellite Pixel, Journal of Geophysical Research: Atmospheres, 123, 6777-6803, https://doi.org/10.1029/2018JD028422, 2018.

Liu, H., Randerson, J. T., Lindfors, J., Massman, W. J., and Foken, T.: Consequences of Incomplete Surface Energy Balance Closure for CO2 Fluxes from Open-Path CO2/H2O Infrared Gas Analysers, Boundary-Layer Meteorology, 120, 65-85, 10.1007/s10546-005-9047-z, 2006.

Liu, J., Chen, J. M., Cihlar, J., and Chen, W.: Net primary productivity distribution in the BOREAS region from a process model using satellite and surface data, Journal of Geophysical Research: Atmospheres, 104, 27735-27754, https://doi.org/10.1029/1999JD900768, 1999.

Liu, S., Xu, Z., Song, L., Zhao, Q., Ge, Y., Xu, T., Ma, Y., Zhu, Z., Jia, Z., and Zhang, F.: Upscaling evapotranspiration measurements from multi-site to the satellite pixel scale over heterogeneous land surfaces, Agricultural and Forest Meteorology, 230-231, 97-113, https://doi.org/10.1016/j.agrformet.2016.04.008, 2016.

Liu, S., Li, X., Xu, Z., Che, T., Xiao, Q., Ma, M., Liu, Q., Jin, R., Guo, J., Wang, L., Wang, W., Qi, Y., Li, H., Xu, T., Ran, Y., Hu, X., Shi, S., Zhu, Z., Tan, J., Zhang, Y., and Ren, Z.: The Heihe Integrated Observatory Network: A Basin-Scale Land Surface Processes Observatory in China, Vadose Zone Journal, 17, 180072, https://doi.org/10.2136/vzj2018.04.0072, 2018.

Mahrt, L.: Flux Sampling Errors for Aircraft and Towers, Journal of Atmospheric and Oceanic Technology, 15, 416-429, https://doi.org/10.1175/1520-0426(1998)015<0416:FSEFAA>2.0.CO;2, 1998.

Massman, W. and Clement, R.: Uncertainty in Eddy Covariance Flux Estimates Resulting from Spectral Attenuation, in: Handbook of Micrometeorology: A Guide for Surface Flux Measurement and Analysis, edited by: Lee, X., Massman, W., and Law, B., Springer Netherlands, Dordrecht, 67-99, 10.1007/1-4020-2265-4_4, 2005.

Mathez, E. and Smerdon, J.: Climate Change3. Ocean– Atmosphere Interactions, in: The Science of Global Warming and Our Energy Future, Columbia University Press, 69-100, doi:10.7312/math17282-005, 2018.

Mauder, M., Cuntz, M., Drüe, C., Graf, A., Rebmann, C., Schmid, H. P., Schmidt, M., and Steinbrecher, R.: A strategy for quality and uncertainty assessment of long-term eddy-covariance measurements, Agricultural and Forest Meteorology, 169, 122-135, https://doi.org/10.1016/j.agrformet.2012.09.006, 2013.

Mayer, J., Mayer, M., Haimberger, L., and Liu, C.: Comparison of Surface Energy Fluxes from Global to Local Scale, Journal of Climate, 35, 4551-4569, 10.1175/JCLI-D-21-0598.1, 2022.

Metzger, S., Junkermann, W., Butterbach-Bahl, K., Schmid, H. P., and Foken, T.: Measuring the 3-D wind vector with a weight-shift microlight aircraft, Atmos. Meas. Tech., 4, 1421-1444, 10.5194/amt-4-1421-2011, 2011.

Metzger, S., Junkermann, W., Mauder, M., Beyrich, F., Butterbach-Bahl, K., Schmid, H. P., and Foken, T.: Eddy-covariance flux measurements with a weight-shift microlight aircraft, Atmos. Meas. Tech., 5, 1699-1717, 10.5194/amt-5-1699-2012, 2012.

Mohan, M. M. P., Rajitha, K., and Murari, R. R. V.: Review of approaches for the estimation of sensible heat flux in remote sensing-based evapotranspiration models, Journal of Applied Remote Sensing, 14, 1-31, 10.1117/1.JRS.14.041501, 2020.

Peltola, O., Aslan, T., Ibrom, A., Nemitz, E., Rannik, Ü., and Mammarella, I.: The high-frequency response correction of eddy covariance fluxes – Part 1: An experimental approach and its interdependence with the time-lag estimation, Atmos. Meas. Tech., 14, 5071-5088, 10.5194/amt-14-5071-2021, 2021.

Prudden, S., Fisher, A., Marino, M., Mohamed, A., Watkins, S., and Wild, G.: Measuring wind with Small Unmanned Aircraft Systems, Journal of Wind Engineering and Industrial Aerodynamics, 176, 197-210, https://doi.org/10.1016/j.jweia.2018.03.029, 2018.

Prueger, J. H., Hatfield, J. L., Parkin, T. B., Kustas, W. P., Hipps, L. E., Neale, C. M. U., MacPherson, J. I., Eichinger, W. E., and Cooper, D. I.: Tower and Aircraft Eddy Covariance Measurements of Water Vapor, Energy, and Carbon Dioxide Fluxes during SMACEX, Journal of Hydrometeorology, 6, 954-960, 10.1175/JHM457.1, 2005.

Rannik, Ü., Peltola, O., and Mammarella, I.: Random uncertainties of flux measurements by the eddy covariance technique, Atmos. Meas. Tech., 9, 5163-5181, 10.5194/amt-9-5163-2016, 2016.

Reineman, B. D., Lenain, L., Statom, N. M., and Melville, W. K.: Development and Testing of Instrumentation for UAV-Based Flux Measurements within Terrestrial and Marine Atmospheric Boundary Layers, Journal of Atmospheric and Oceanic Technology, 30, 1295-1319, 10.1175/JTECH-D-12-00176.1, 2013.

Reuder, J., Båserud, L., Jonassen, M. O., Kral, S. T., and Müller, M.: Exploring the potential of the RPA system SUMO for multipurpose boundary-layer missions during the BLLAST campaign, Atmos. Meas. Tech., 9, 2675-2688, 10.5194/amt-9-2675-2016, 2016.

Sayres, D. S., Dobosy, R., Healy, C., Dumas, E., Kochendorfer, J., Munster, J., Wilkerson, J., Baker, B., and Anderson, J. G.: Arctic regional methane fluxes by ecotope as derived using eddy covariance from a low-flying aircraft, Atmos. Chem. Phys., 17, 8619-8633, 10.5194/acp-17-8619-2017, 2017.

Serrano-Ortiz, P., Kowalski, A. S., Domingo, F., Ruiz, B., and Alados-Arboledas, L.: Consequences of Uncertainties in CO2 Density for Estimating Net Ecosystem CO2 Exchange by Open-path Eddy Covariance, Boundary-Layer Meteorology, 126, 209-218, 10.1007/s10546-007-9234-1, 2008.

Sun, Y., Jia, L., Chen, Q., and Zheng, C.: Optimizing Window Length for Turbulent Heat Flux Calculations from Airborne Eddy Covariance Measurements under Near Neutral to Unstable Atmospheric Stability Conditions, Remote Sensing, 10, 10.3390/rs10050670, 2018.

Sun, Y., Ma, J., Sude, B., Lin, X., Shang, H., Geng, B., Diao, Z., Du, J., and Quan, Z.: A UAV-Based Eddy Covariance System for Measurement of Mass and Energy Exchange of the Ecosystem: Preliminary Results, Sensors, 21, 10.3390/s21020403, 2021a.

Sun, Y., Sude, B., Geng, B., Ma, J., Lin, X., Hao, Z., Jing, W., Chen, Q., and Quan, Z.: Observation of the winter regional evaporative fraction using a UAV-based eddy covariance system over wetland area, Agricultural and Forest Meteorology, 310, 108619, https://doi.org/10.1016/j.agrformet.2021.108619, 2021b.

Thomas, R. M., Lehmann, K., Nguyen, H., Jackson, D. L., Wolfe, D., and Ramanathan, V.: Measurement of turbulent water vapor fluxes using a lightweight unmanned aerial vehicle system, Atmos. Meas. Tech., 5, 243-257, 10.5194/amt-5-243-2012, 2012.

van den Kroonenberg, A., Martin, T., Buschmann, M., Bange, J., and Vörsmann, P.: Measuring the Wind Vector Using the Autonomous Mini Aerial Vehicle M2AV, Journal of Atmospheric and Oceanic Technology, 25, 1969-1982, 10.1175/2008JTECHA1114.1, 2008.

van den Kroonenberg, A. C., Martin, S., Beyrich, F., and Bange, J.: Spatially-Averaged Temperature Structure Parameter Over a Heterogeneous Surface Measured by an Unmanned Aerial Vehicle, Boundary-Layer Meteorology, 142, 55-77, 10.1007/s10546-011-9662-9, 2012.

Vellinga, O. S., Dobosy, R. J., Dumas, E. J., Gioli, B., Elbers, J. A., and Hutjes, R. W. A.: Calibration and Quality Assurance of Flux Observations from a Small Research Aircraft*, Journal of Atmospheric and Oceanic Technology, 30, 161-181, 10.1175/JTECH-D-11-00138.1, 2013.

Vellinga, O. S., Gioli, B., Elbers, J. A., Holtslag, A. A. M., Kabat, P., and Hutjes, R. W. A.: Regional carbon dioxide and energy fluxes from airborne observations using flight-path segmentation based on landscape characteristics, Biogeosciences, 7, 1307-1321, 10.5194/bg-7-1307-2010, 2010.

Wang, H., Jia, G., Zhang, A., and Miao, C.: Assessment of Spatial Representativeness of Eddy Covariance Flux Data from Flux Tower to Regional Grid, Remote Sensing, 8, 742, 2016.

Webb, E. K., Pearman, G. I., and Leuning, R.: Correction of flux measurements for density effects due to heat and water vapour transfer, Quarterly Journal of the Royal Meteorological Society, 106, 85-100, https://doi.org/10.1002/qj.49710644707, 1980.

Williams, A. and Marcotte, D.: Wind Measurements on a Maneuvering Twin-Engine Turboprop Aircraft Accounting for Flow Distortion, Journal of Atmospheric and Oceanic Technology, 17, 795-810, 10.1175/1520-0426(2000)017<0795:WMOAMT>2.0.CO;2, 2000.

Witte, B. M., Singler, R. F., and Bailey, S. C. C.: Development of an Unmanned Aerial Vehicle for the Measurement of Turbulence in the Atmospheric Boundary Layer, Atmosphere, 8, 10.3390/atmos8100195, 2017.

Wolfe, G. M., Kawa, S. R., Hanisco, T. F., Hannun, R. A., Newman, P. A., Swanson, A., Bailey, S., Barrick, J., Thornhill, K. L., Diskin, G., DiGangi, J., Nowak, J. B., Sorenson, C., Bland, G., Yungel, J. K., and Swenson, C. A.: The NASA Carbon Airborne Flux Experiment (CARAFE): instrumentation and methodology, Atmos. Meas. Tech., 11, 1757-1776, 10.5194/amt-11-1757-2018, 2018.

Xu, S., Xu, S., Zhou, Y., Yue, S., Zhang, X., Gu, R., Zhang, Y., Qiao, Y., and Liu, M.: Long-Term Changes in the Unique and Largest Seagrass Meadows in the Bohai Sea (China) Using Satellite (1974–2019) and Sonar Data: Implication for Conservation and Restoration, Remote Sensing, 13, 856, 10.3390/rs13050856, 2021.

Yang, X., Yong, B., Ren, L., Zhang, Y., and Long, D.: Multi-scale validation of GLEAM evapotranspiration products over China via ChinaFLUX ET measurements, International Journal of Remote Sensing, 38, 5688-5709, 10.1080/01431161.2017.1346400, 2017.

Zhang, G., Zhang, J., and Meng, P.: Estimation of kilometer-scale heat fluxes over a hilly area in Northern China using an optical-microwave scintillometer, Agricultural Water Management, 244, 106582, https://doi.org/10.1016/j.agwat.2020.106582, 2021.

Zheng, C., Liu, S., Song, L., Xu, Z., Guo, J., Ma, Y., Ju, Q., and Wang, J.: Comparison of sensible and latent heat fluxes from optical-microwave scintillometers and eddy covariance systems with respect to surface energy balance closure, Agricultural and Forest Meteorology, 331, 109345, https://doi.org/10.1016/j.agrformet.2023.109345, 2023.